

## The effect of biofilms on turbulent flow over permeable beds

Kazemifar, F; Blois, G; Aybar, M; Perez Calleja, P; Nerenberg, R; Sinha, S; Hardy, RJ; Best, JL; Sambrook-Smith, Greg; Christensen, KT

DOI:  
[10.1029/2019WR026032](https://doi.org/10.1029/2019WR026032)

License:  
None: All rights reserved

*Document Version*  
Peer reviewed version

*Citation for published version (Harvard):*  
Kazemifar, F, Blois, G, Aybar, M, Perez Calleja, P, Nerenberg, R, Sinha, S, Hardy, RJ, Best, JL, Sambrook-Smith, G & Christensen, KT 2021, 'The effect of biofilms on turbulent flow over permeable beds', *Water Resources Research*, vol. 57, no. 2, e2019WR026032. <https://doi.org/10.1029/2019WR026032>

[Link to publication on Research at Birmingham portal](#)

### **Publisher Rights Statement:**

An edited version of this paper was published by AGU. Copyright 2020 American Geophysical Union.

Kazemifar, F., Blois, G., Aybar, M., Perez Calleja, P., Nerenberg, R., Sinha, S., et al. (2021). The effect of biofilms on turbulent flow over permeable beds. *Water Resources Research*, 57, e2019WR026032. To view the published open abstract, go to: <https://doi.org/10.1029/2019WR026032>

### **General rights**

Unless a licence is specified above, all rights (including copyright and moral rights) in this document are retained by the authors and/or the copyright holders. The express permission of the copyright holder must be obtained for any use of this material other than for purposes permitted by law.

- Users may freely distribute the URL that is used to identify this publication.
- Users may download and/or print one copy of the publication from the University of Birmingham research portal for the purpose of private study or non-commercial research.
- User may use extracts from the document in line with the concept of 'fair dealing' under the Copyright, Designs and Patents Act 1988 (?)
- Users may not further distribute the material nor use it for the purposes of commercial gain.

Where a licence is displayed above, please note the terms and conditions of the licence govern your use of this document.

When citing, please reference the published version.

### **Take down policy**

While the University of Birmingham exercises care and attention in making items available there are rare occasions when an item has been uploaded in error or has been deemed to be commercially or otherwise sensitive.

If you believe that this is the case for this document, please contact [UBIRA@lists.bham.ac.uk](mailto:UBIRA@lists.bham.ac.uk) providing details and we will remove access to the work immediately and investigate.

## **The Effect of Biofilms on Turbulent Flow over Permeable Beds**

**Farzan Kazemifar<sup>1</sup>, Gianluca Blois<sup>2</sup>, Marcelo Aybar<sup>3\*</sup>, Patricia Perez Calleja<sup>3</sup>, Robert Nerenberg<sup>3</sup>, Sumit Sinha<sup>4‡</sup>, Richard J. Hardy<sup>4</sup>, James L. Best<sup>5</sup>, Gregory H. Sambrook Smith<sup>6</sup>, Kenneth T. Christensen<sup>2,3,7</sup>**

<sup>1</sup>Department of Mechanical Engineering, San Jose State University, USA. <sup>2</sup>Department of Aerospace and Mechanical Engineering, University of Notre Dame, USA. <sup>3</sup>Department of Civil and Environmental Engineering and Earth Sciences, University of Notre Dame, USA. <sup>4</sup>Department of Geography, Durham University, UK. <sup>5</sup>Departments of Geology, Geography and GIS, Mechanical Science and Engineering and Ven Te Chow Hydrosystems Laboratory, University of Illinois at Urbana-Champaign, USA. <sup>6</sup>School of Geography, Earth and Environmental Sciences, University of Birmingham, UK. <sup>7</sup>International Institute for Carbon Neutral Energy Research (I<sup>2</sup>CNER), Kyushu University, Japan.

Corresponding author: Kenneth Christensen ([christensen.33@nd.edu](mailto:christensen.33@nd.edu))

\*Current address: Department of Civil Engineering, Universidad de Concepción, Chile.

‡Current address: School of Earth and Environment, University of Leeds, UK.

### **Key Points:**

- The effect of presence of biofilm on turbulence in the free flow is due to a combination of reduced bed porosity and change in geometry and roughness.
- Presence of biofilm increases Reynolds stresses in the outer layer scaling with wall shear stress.
- Presence of biofilm dampens dimensionless Reynolds stresses in the vicinity of the permeable bed.

## Abstract

In nearly all aquatic, and many industrial environments, colonization of bacteria on solid surfaces results in microbial growth in the form of biofilms, consisting of a collection of microscopic organisms living in a self-secreted polymeric matrix. The growth and detachment of biofilms are coupled to flow hydrodynamics and turbulence. In alluvial channels, a typical substrate consists of a rough permeable bed where biofilm presence modifies both bed porosity and surface roughness, thereby altering mass and momentum exchange at the bed interface. While there is literature detailing turbulent flow over permeable media, little is known concerning how such flow may be affected by the presence of biofilms. This paper addresses this challenge by quantifying the effects of biofilms on flow over laboratory permeable beds with idealized geometry and conditions using particle image velocimetry. The wall shear stress and friction velocity obtained from the total shear stress increased in the presence of biofilm, and decreased as a result of biofilm detachment, when compared at constant pump frequency. The dimensionless Reynolds stresses, at constant pump frequency, collapsed for different bed configurations in the outer layer, while for the inner layer, the presence of biofilm led to a decrease in dimensionless Reynolds stress. Quadrant analysis showed that this decrease was primarily due to a reduction in strong Q2 contributions. These results suggest that models for flow and transport over permeable media in aquatic environments cannot neglect the role of biofilms in modifying turbulence.

## 1 Introduction

Flows over porous media are central to key biogeochemical processes occurring in many natural and industrial aquatic systems. In particular, exchange of mass, momentum, nutrients and heat in the hyporheic zone is central to many hydrologic systems (Cardenas 2015; Packman and Bencala 2000; Sternecker, Wild, and Geist 2013). In alluvial channels, for example, recent studies have shown that bed porosity results in the generation of a diverse mosaic of turbulent suction and ejection events that are fundamentally different from those occurring over impermeable walls (Blois et al. 2011, 2014; Kim et al. 2018; Manes, Pokrajac, et al. 2011; Sinha et al. 2017; Stoesser and Rodi 2007; Suga et al. 2010). Knowledge of these dynamics, at a range of scales, is important due to their critical role in sedimentation, as well as transport of nutrients, pollutants, and dissolved oxygen (Boano et al., 2014; Grant, Gomez-Velez, and Ghisalberti 2018; Roche et al., 2018). Turbulent flow over permeable walls has been studied using both experiments (Blois et al., 2012; Kim et al., 2018, 2019, 2020; Manes et al., 2009; Manes et al., 2011a; Manes et al., 2011b; Pokrajac and Manes 2009; Roche et al., 2018; Suga et al., 2010; Suga et al., 2017) and numerical simulations (Breugem and Boersma 2005; Breugem et al., 2006; Rosti et al., 2015; Sinha et al., 2017). In these studies, the effects of wall permeability on the structure and dynamics of turbulence across the permeable interface, as well as the link between turbulence inside and outside the wall, have been studied. Four important modifications have been highlighted compared to flows over impermeable walls with similar interfacial topography: 1) an earlier transition to turbulence (Suga et al., 2010), 2) increased bulk flow resistance, 3) increased Reynolds shear stress (RSS) contributions from sweep events in the immediate vicinity of the permeable wall (Suga et al., 2011), and 4) enhanced turbulence due to bed permeability. While these studies provide a wealth of new understanding concerning the physics of turbulent flows overlying permeable walls, they have focused on a static wall geometry rather than a dynamic wall interface, where the geometry can be altered by processes such as microorganism colonization over a range of timescales. For example, the total biomass, and hence porosity, of the interface may change with the seasons, or at much smaller

scales as individual biofilm streamers move in response to turbulence and that can lead to short-lived fluctuations in the interface porosity.

In almost all aquatic environments, as a result of attachment and colonization of bacteria on solid surfaces, microbial biomass exists in the form of biofilms consisting of a collection of different microscopic organisms living in a self-secreted polymeric matrix (Battin et al., 2007), and that can have profound effects on the flow dynamics. The presence of biofilms can alter flow structure in a number of ways, such as reduced bed porosity due to the presence of biomass in the pores and throats of the porous bed. Previous studies have shown decreased velocity fluctuations and Reynolds shear stresses with reduced bed porosity (Breugem et al., 2006; Rosti et al., 2015). In addition, the biofilm can modify the geometry of the porous matrix, which is particularly important at the interface between the subsurface and free-flow where changes in surface roughness can affect the flow structure. The combined effects from these factors result in a modified flow structure for flow over biofilm-covered permeable beds.

Biofilm growth may stabilize sediments and alter the mechanism of sediment entrainment, as well as influencing the generation of bedforms (Lichtman et al. 2018; Malarkey et al. 2015; Parsons et al. 2016). Vignaga et al. (2013) showed that bio-stabilized sediment (i.e. biofilm-bound sediment) acts more like a stretched membrane than a collection of loose particles. In gravel-bed rivers, biofilm growth can affect the hydrodynamics of flow and hyporheic exchange by modifying the geometry of the bed interface and the connectivity of subsurface pore spaces. This can, in turn, affect the concentration of oxygen, organic carbon, and other electron acceptors, as well as the biogeochemical reactions occurring inside the bed (Battin et al. 2003; Boano et al. 2014; Dzubakova et al. 2018). However, a limited number of studies have addressed quantitatively the effects of biofilm on flow characteristics, particularly for flow over permeable surfaces. Graba et al. (2010) quantified biomass dynamics during growth and subsequent detachment stages of epilithic biofilms on impermeable rough beds with 20-mm-high hemispherical artificial cobbles in a turbulent flow. They reported a modest decrease in bed shear stress and a decrease in equivalent sand grain roughness due to smoothing of bottom roughness from biofilm growth. In a follow-up study, Graba et al. (2013) investigated the effect of flow rate and wall shear stress on biomass dynamics and the algal composition of biofilm during growth and detachment stages. They observed a similar trend in wall shear stress with biofilm growth and also reported a direct relationship between biofilm attachment strength and shear stress during biofilm growth. Walker et al. (2013) studied the modification of a turbulent boundary layer developing over a biofilm-covered smooth impermeable surface, such as would relate to the drag on a ship hull. They reported increased skin friction due to biofilm growth on smooth walls. Moreover, a notable finding from their study was that the effective equivalent sand grain roughness of biofilms was greater than their physical roughness, owing to their compliant structure and resulting motion under turbulent flow conditions. In another group of studies, the effect of the presence and growth of biofilm on transport phenomena over and inside porous media has been investigated, showing increased dispersion, longer retention times, and non-Fickian transport with biofilm growth (Aubeneau et al., 2016; Carrel et al., 2018; Roche et al., 2017).

Thus, while biofilms are ubiquitous in aquatic environments and exist on almost all wet surfaces, their effect on flow over permeable walls is poorly understood. This lack of direct measurements represents a knowledge gap that limits our ability to develop reliable predictive models of flow

over environmental systems such as gravel bed rivers, which are highly permeable and typically a location for biofilm growth. In the present study, we aim to investigate experimentally the effects of presence of biofilm on flow over idealized permeable beds. To this end, we use particle image velocimetry (PIV) to quantify the characteristics of transitional and turbulent flow over permeable beds with and without biofilms.

## 2 Experimental Apparatus

### 2.1 Flow Facility

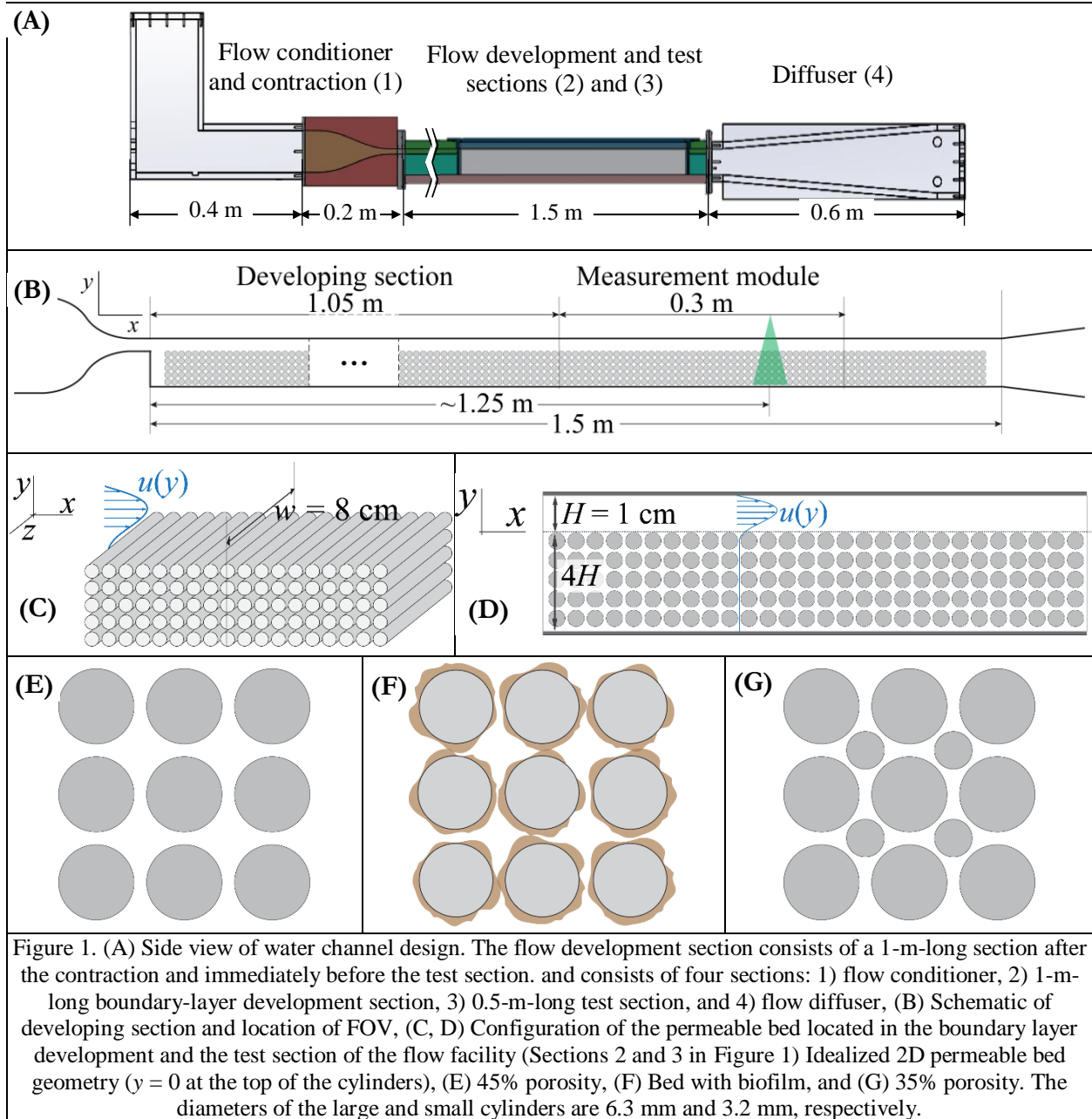
A special flow facility was designed and built to accommodate the use of permeable beds with different geometries. The flow facility was a recirculating closed water channel with rectangular cross-section (Figure 1A and B), and consisted of four sections: 1) flow conditioner, 2) boundary-layer development section, 3) test section, and 4) flow diffuser. In order to reduce the turbulence intensity of the incoming flow, the flow conditioner was equipped with a perforated plastic sheet, 3 mesh screens, and a two-dimensional contraction section with inlet to outlet height ratio of 8:1. The boundary-layer development section was 1 m in length followed by the 0.50-m-long test section equipped with glass windows on the two side walls as well as the top wall for optical access. Flow rate was controlled by setting the pump frequency,  $f$ , using a variable frequency drive, and discharge was measured using a SeaMetrics EX810P insertion electromagnetic flow meter.

The permeable bed consisted of a regular array of acrylic rods spanning the width of the channel covering both the boundary layer development section and the test section (sections (2) and (3) in Figure 1A). The acrylic rods were secured to two machined perforated acrylic plates with holes for the rods (similar to a peg board). The bed consisted of four 0.30-m-long individual sections plus two 0.15-m-long sections to accommodate the transition after the contraction and before the diffuser. The design of these perforated plates allowed the rods to be mounted in two different arrangements and thus two different porosities of 35% and 45%. As shown in Figure 1, the higher porosity was achieved using 6.3 mm (0.25 in) acrylic rods mounted in a square array, while the lower porosity was achieved by adding 3.2 mm (0.125 in) acrylic rods to the center of each square cell, thus reducing the porosity by ~10%. The value for the lower porosity was primarily determined based on cost and manufacturability constraints, yet its porosity was also representative of gravel riverbeds.

## 2.2 Biofilm Growth Reactor

### 2.2.1 Biofilm Reactor

A dedicated recirculating reactor was designed and built to grow biofilm on the measurement module of the permeable bed under controlled conditions. The measurement module was a 0.30-m-long section of the permeable bed that was transferred to the water channel and placed in the test section for flow experiments after biofilm growth. The decision to develop biofilm *outside* the flow facility, and in a standalone biofilm reactor, was made to avoid undesired biofilm growth in portions of the water channel with limited access for cleaning. In this regard, biofilm growth on the top wall in the boundary layer development section could have had unpredictable effects on the flow characteristics in the channel. Due to this choice, there was a transition in bed porosity at the beginning of the test section that resulted in developing flow over the biofilm bed in the test section.



### 2.2.2 Biofilm Development Protocol

Figure 2A shows schematically the configuration of the reactor. A multi-cassette Cole Parmer MasterFlex L/S peristaltic pump (P1) was used to deliver the electron donor and growth medium at fixed equal flow rates of 4 ml/min. A 250-g/m<sup>3</sup> aqueous solution of potassium acetate (KCH<sub>3</sub>COO) was used as the electron donor and tap water was used as the growth medium due to its high mineral concentration. A Cole Parmer gear pump (P2) was used for recirculation of the fluids at 40× the combined influent and effluent flow rate (~320 ml/min) to establish fully mixed conditions in the reactor. The resulting average streamwise flow velocity in the reactor, based on the volumetric flow rate and the cross-sectional area, was ~4 mm/s. A third cassette on the peristaltic pump was used to extract the effluent from the aeration bottle and maintain a constant fluid level therein. An aeration stone inside the aeration bottle was connected to a low-pressure air

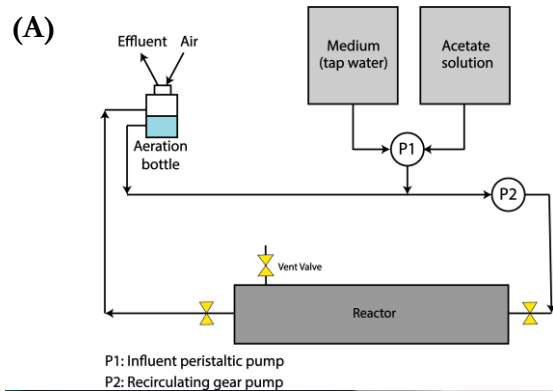
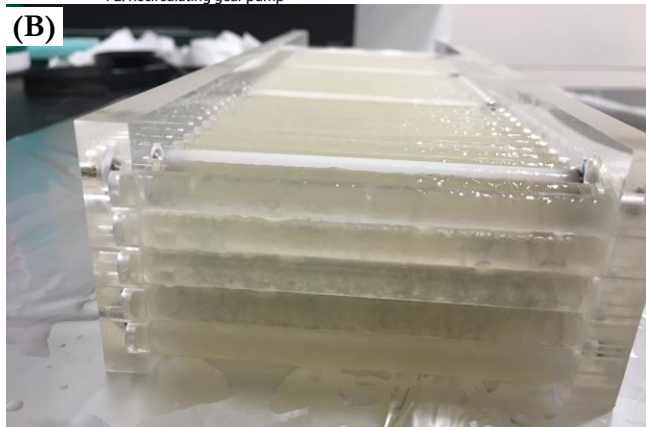


Figure 2. Flow diagram for the recirculating biofilm reactor (A). Biofilm bed section removed from the reactor before being transferred to the flow facility (B), (C). A multi-cassette Cole Parmer MasterFlex L/S peristaltic pump (P1) was used to deliver the electron donor and growth medium solutions. A Cole Parmer gear pump (P2) was used for recirculation of the fluids to establish fully-mixed conditions in the reactor.



supply line to provide oxygen to the reactor. In this manner, the dissolved oxygen levels were maintained close to saturation and thus compensated for oxygen consumption by biofilm activity.

The reactor, with the measurement module of the permeable bed placed inside, was inoculated with activated sludge from a local wastewater treatment plant. Biofilm was allowed to grow on the cylinders for 14 days. During this time period, the biofilm was exposed to room light for approximately 6–10 hours each day. Based on the inoculum and growth conditions, the dominant members in this biofilm were heterotrophic and nitrifying bacteria whose growth is relatively insensitive to light conditions. The reactor was maintained at the room temperature of 20–22°C. After the 14-day growth period, the biofilm-covered measurement module was removed from the reactor and its sidewalls above the top layer of the cylinders were cleaned carefully without disturbing the biofilm to ensure unhindered optical access. This module was then transferred to the flow facility for flow experiments. Figure 2B and C show the biofilm-covered bed before being placed in the water channel. It is worth noting that the biofilm growth was limited to the reactor-processed portion of the bed section, and thus a sharp transition in terms of bed porosity and roughness geometry existed at the ends of this section. The effect of this transition on flow development is discussed in §5.

### 2.3 PIV Setup

A dual-head, pulsed, Evergreen Nd:YAG laser with maximum energy of 200 mJ/pulse was used to form a ~1-mm-thick laser sheet to illuminate the tracer particles in the streamwise–wall-normal ( $x$ – $y$ ) plane. The longitudinal position of the light sheet was 1.25 m downstream of the channel inlet and approximately 0.20 m from the beginning of the measurement module (Figure 1B), and

its spanwise ( $z$ -direction, Figure 1C) position was equidistant from the two side walls. A 16-bit, Andor Neo sCMOS camera with 5.5-megapixel ( $2560 \times 2160$ -pixel array) sensor and a pixel size of  $6.5 \mu\text{m}$  was used to capture image pairs at a rate of 10 Hz. The camera was coupled with a Navitar long-distance microscope with numerical aperture (NA) of  $\sim 0.012$ , consisting of a  $0.25\times$  objective, a  $2\times$  adapter, and a zoom lens set at  $\sim 2\times$  resulting in a magnification of  $\sim 1.1\times$  translating to  $\sim 7 \mu\text{m}/\text{pixel}$ , and a resolution of  $\sim 40 \mu\text{m}$  at 550 nm wavelength. The field of view of the imaging setup was  $\sim 18 \times 14 \text{ mm}^2$ . The FOV covered up to  $\sim 7 \text{ mm}$  above the cylinder tops, in order to avoid error from optical aberrations observed near the top of the FOV. Fluorescent particles  $\sim 10\text{-}15 \mu\text{m}$  in diameter were introduced into the flow as tracers and their fluoresced light was recorded using a long-pass 550 nm filter. Raw PIV images were processed with LaVision DaVis 8.2 software using a sequential cross-correlation algorithm with a final interrogation window size of  $64^2$  pixels with 50% overlap, resulting in a vector field resolution of  $\sim 0.44 \text{ mm}$  and a vector grid spacing of  $\sim 0.22 \text{ mm}$  ( $0.035d$ ).

## 2.4 Experiments

Five sets of experiments were conducted – two without biofilm (*nBF*) and three with biofilm-covered bed sections (*BF*). The reference case is taken as flow over the bed with 45% porosity throughout the channel without biofilm (*nBF*-45%). The other dataset without biofilm was *nBF*-45-35% where the bed porosity is 45% in the developing section leading to a 0.30-m-long section with 35% porosity. Lastly, the *BF* datasets correspond to experiments on different batches of biofilm developed independently at different times. The bed porosity in the channel was 45% leading to 30-m-long biofilm-covered section, whose bed porosity was presumably smaller than 45% due to presence of biomass. Details of the experimental beds are presented in Table 1.

Table 1. Dataset Summary

Dataset	Biofilm	Description
<i>nBF</i> -45% (reference)	No	45% bed porosity in the boundary-layer development and test section
<i>nBF</i> -45-35%	No	45% bed porosity in the boundary-layer development section, and 35% porosity in the test section.
<i>BF1</i>	Yes	45% bed porosity in clean conditions (before biofilm growth; the <i>actual</i> porosity in the biofilm section is likely lower due to presence of biofilm). These correspond to three different batches of biofilm developed independently at different times in the same reactor.
<i>BF2</i>	Yes	
<i>BF3</i>	Yes	

Temporal decomposition of the velocity field,  $\mathbf{u}(x,y,t) = (u(x,y,t), v(x,y,t))$ , was performed as  $u = \bar{u} + u'$ , where the overbar denotes time-averaged (Reynolds-averaged or mean) values and the prime denotes the deviation from the time-averaged value. Line averaging in the streamwise direction ( $x$ -direction) at any vertical position  $y$ , was performed according to the definition given by Nikora et al. (2001). For example, for mean streamwise velocity,  $\bar{u}$ :

$$\langle \bar{u} \rangle(y) = \left( \int_{A_f} \bar{u}(x', y) dx' \right) / A_f \quad (1)$$

where  $A_f$  is the area occupied by fluid at any vertical position,  $y$ , and is determined based on the number of vectors at each  $y$  location. Also, spatial deviation is calculated as the difference between the time-averaged and doubled-averaged quantities.  $\tilde{u} = \bar{u} - \langle \bar{u} \rangle$ .



Figure 3 shows a representative time-averaged velocity field, with streamwise velocity  $\bar{u}$  contours and streamlines (Figure 3A), in addition to the corresponding double-averaged velocity profile,  $\langle \bar{u} \rangle(y)$ , (Figure 3B). Due to flow detachment, a recirculation region exists between the cylinders that results in negative streamwise velocities with a velocity magnitude of  $\sim 0.1 U_{max}$ . Similar to observations by Breugem et al., (2006), the line-averaged velocity profile,  $\langle \bar{u} \rangle$ , exhibits an inflection point just below the interface, denoted as  $y_{inflec}$ . The PIV uncertainty in particle displacement calculated from the images is 5% of particle image diameter, or  $\sim 0.1$  pixels ( $\sim 1.4 \times 10^{-3}$  mm in the measurement plane). For the different laser pulse time delays used herein, this equates to a velocity uncertainty of  $\sim 0.4\%$  of  $U_{max}$  in each case.

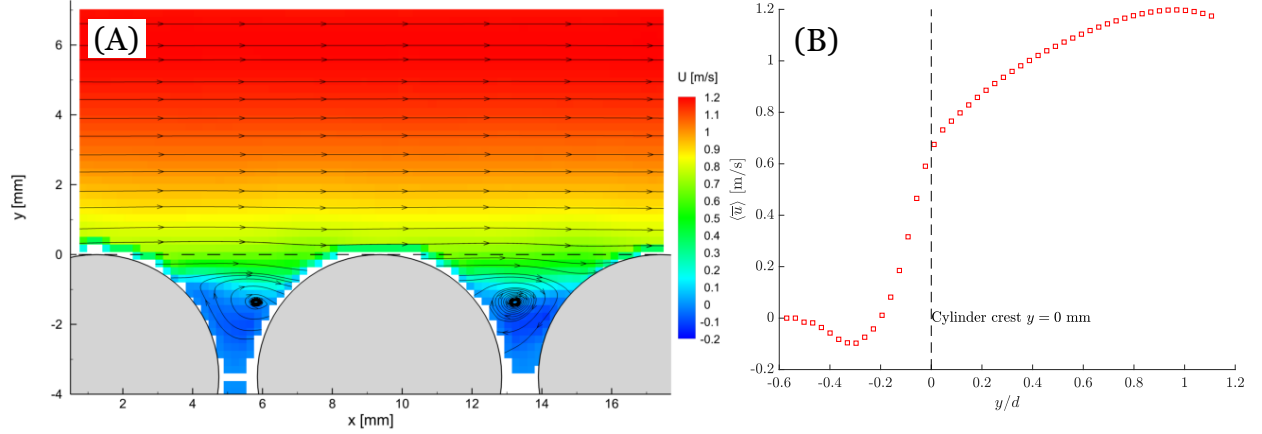


Figure 3. (A) Time-averaged streamwise velocity,  $\bar{u}$ , (B) double-averaged velocity profile at  $Re \approx 7000$ . Dashed line indicates the top of the cylinders at  $y = 0$  mm, and  $d = 6.3$  mm is the cylinder diameter.

The total shear stress,  $\tau$ , is calculated as the sum of viscous, Reynolds, and dispersive (form-induced) shear stresses:

$$\tau = \mu \frac{d\langle \bar{u} \rangle}{dy} - \rho \langle u'v' \rangle - \rho \langle \tilde{u}\tilde{v} \rangle. \quad (2)$$

Figure 4 presented the total shear stress as well as the individual terms from Eq. (2), normalized with wall shear stress  $\tau_w^p$ . The shear stress does not include the drag term below the cylinder crest ( $y/d < 0$ ). The shear stress at the permeable wall,  $\tau_w^p$ , was calculated by extrapolating the linear segment of the total shear stress profile (Eq. (2) with density,  $\rho = 997.5 \text{ kg/m}^3$  and viscosity,  $\mu = 0.9321 \times 10^{-3} \text{ Pa.s}$ ) near the channel centerline to the crest location ( $y = 0$ ).

Table 2 presents details of the experimental conditions for different runs and datasets. Discharge,  $Q$ , was directly measured by the flowmeter, while  $U_{max}$ ,  $y_{max}$  and were obtained

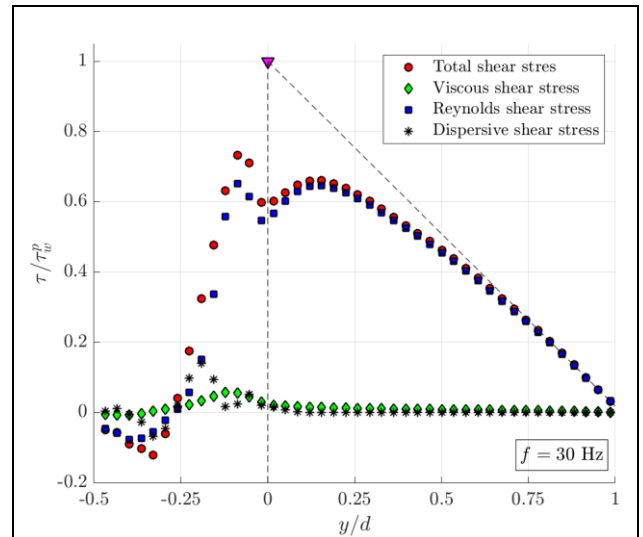


Figure 4. Example of contributions of individual terms to total shear stress and extrapolation for wall shear stress calculation.

from the double-averaged velocity profiles. The bulk Reynolds number,  $Re$ , for this flow configuration is defined as:

$$Re = \frac{U_b H}{\nu}, \quad (3)$$

where  $H$  is the channel height (0.01 m for all cases),  $\nu = 0.934 \times 10^{-3} \text{ m}^2/\text{s}$  is the kinematic viscosity of water, and  $U_b$  is the bulk velocity calculated as the average velocity for  $y \in [0, H]$ , as defined by Breugem et al. (2006). Since the velocity field is resolved up to  $y \approx 7 \text{ mm}$ , a fourth order polynomial curve fit is used to approximate the velocity profile up to the top wall for calculation of  $U_b$ . The friction velocity ( $u_\tau^p$ ) and friction Reynolds number ( $Re_\tau^p$ ) are defined as:

$$u_\tau^p = \sqrt{\tau_w^p / \rho}, \quad (4)$$

$$Re_\tau^p = \frac{u_\tau^p H}{\nu}. \quad (5)$$

The permeability Reynolds number ( $Re_K$ ) is calculated as,

$$Re_K = \frac{u_\tau^p \sqrt{K}}{\nu} \quad (6)$$

where  $K$  is the bed permeability estimated from the Kozeny-Carman equation for cylinders in cross-flow (Nakayama, Kuwahara, and Sano 2007),

$$K = \frac{\phi^3 d_h^2}{144(1 - \phi)^2} \quad (7)$$

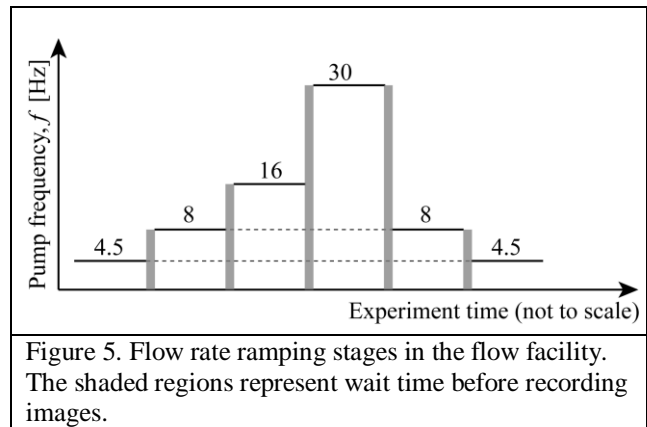
where  $\phi$  is porosity and  $d_h$  is the pore hydraulic diameter. This yields a permeability of  $0.087 \text{ mm}^2$  and  $0.051 \text{ mm}^2$  for the bed with 45% and 35% porosity, respectively. As a first approximation for the bed with biofilm, we used the same permeability value as the low-porosity bed.

For sufficiently high Reynolds number, a logarithmic layer is expected in the boundary layer above the permeable bed. A common parametrization of the log law is

$$\langle \bar{u} \rangle^+ = \frac{1}{\kappa} \ln \left( \frac{y^+ + y_0^+}{k_s^+} \right), \quad (8)$$

where  $\langle \bar{u} \rangle^+ = \langle \bar{u} \rangle / u_\tau^p$ , and  $\kappa$  is the equivalent to the von Karman constant (Breugem et al. 2006; Fang et al. 2018). Also,  $y^+$  is the vertical distance above the cylinder crest,  $y_0^+$  is the zero-displacement height, and  $k_s^+$  is the equivalent roughness height, all normalized with viscous length scale  $y^* = \nu / u_\tau^p$ .

In experiments with biofilm, the pump frequency,  $f$ , and channel flow rate,  $Q$ , were increased in steps, and data were recorded for  $f = 4.5 \text{ Hz}$  and  $8 \text{ Hz}$  ( $Q \approx 0.18$  and  $0.28 \text{ L/s}$ ), before reaching the target of  $16 \text{ Hz}$  and  $30 \text{ Hz}$  ( $Q \approx 0.54$  and  $0.95 \text{ L/s}$ ). After recording data for the highest flow rate, the pump frequency was reduced, and data was recorded sequentially at  $f = 8 \text{ Hz}$  and  $4.5 \text{ Hz}$  ( $Q \approx 2.8 \text{ L/s}$  and  $Q \approx 0.18 \text{ L/s}$ ) (with the exception of the *BF3* dataset). Figure 5 illustrates the flow rate ramping stages



schematically. The number of image pairs for each flow setting and the corresponding number of flow-through times is given in Table 3. The flow-through time is calculated as the ratio of the streamwise length (18 mm) of the field of view to the bulk velocity ( $U_b$ ). After each stage, there was at least a 2-minute wait time before recording images. The flow characteristics during ramp up and ramp-down, referred to as *before detachment* (BD) and *after detachment* (AD), respectively, are compared later to illustrate the effect of biofilm detachment on flow behavior.

Table 2. Experimental conditions:  $f$  is pump frequency,  $Q$  is volumetric flow rate,  $U_b$  is bulk velocity,  $U_{max}$  is maximum streamwise velocity,  $y_{max}$  is the coordinate where  $U_{max}$  occurs,  $u_\tau^p$  is the friction velocity at the permeable wall (Eq. 4),  $Re$  is the bulk Reynolds number (Eq. 2), and  $Re_\tau^p$  is the friction Reynolds number at the permeable wall (Eq. 5), and  $Re_K$  is the permeability Reynolds number (Eq. 6).  $k_s^+$ ,  $y_0^+$  and  $\kappa$  are the equivalent roughness height and zero displacement height (normalized with viscous wall units  $y^*$ ) and von Karman constant, respectively, from the logarithmic fit to velocity profile (Eq. 8). BD and AD indicate “before detachment” and “after detachment”, respectively.

Dataset	$f$ [Hz]	$Q$ [L/s]	$U_b$ [m/s]	$U_{max}$ [m/s]	$y_{max}$ [mm]	$u_\tau^p \times 10^{-3}$ [m/s]	$Re$	$Re_\tau^p$	$Re_K$	$k_s^+$	$y_0^+$	$\kappa$
nBF-45%	4.5	0.173	0.150	0.186	5.3	14.1	1610	150	4.4	0.4	4.5	0.40
	8	0.293	0.259	0.315	5.9	24.5	2770	262	7.7	2.9	28.3	0.31
	16	0.534	0.503	0.615	6.2	46.7	5390	500	14.8	13.4	81.0	0.25
	30	0.971	0.977	1.198	6.2	82.1	10460	879	26.0	23.7	141	0.22
nBF-45-35%	4.5	0.177	0.152	0.191	5.2	14.3	1630	153	3.5	0.9	13.2	0.33
	8	0.293	0.267	0.322	5.6	23.2	2860	249	5.6	3.2	33.8	0.28
	16	0.536	0.521	0.639	6.0	46.6	5580	499	11.2	13.1	88.8	0.24
	30	0.953	0.985	1.217	6.0	89.3	10540	956	21.6	35.9	180	0.22
BF1	BD 4.5	0.177	0.167	0.213	5.9	20.1	1790	215	4.9	5.5	28.4	0.31
	BD 8	0.284	0.296	0.379	6.6	35.2	3170	377	8.5	14.0	52.7	0.28
	16	0.543	0.582	0.757	6.8	69.1	6230	739	16.7	60.9	153	0.21
	30	0.953	1.105	1.403	6.6	106	11840	1137	25.6	50.4	173	0.21
	AD 8	0.291	0.297	0.368	6.3	29.3	3180	314	7.1	4.1	30.7	0.31
	AD 4.5	0.173	0.166	0.209	5.7	15.9	1780	170	3.8	0.4	3.4	0.41
BF2	BD 4.5	0.178	0.162	0.205	5.6	17.7	1730	189	4.3	4.3	29.9	0.29
	BD 8	0.281	0.283	0.355	6.0	32.0	3030	343	7.7	13.6	68.6	0.26
	16	0.536	0.563	0.701	6.3	58.7	6030	629	14.2	39.6	165	0.21
	30	0.953	1.029	1.296	6.3	102	11020	1093	24.6	44.4	208	0.23
	AD 8	0.287	0.280	0.344	5.8	26.2	3000	281	6.3	5.9	51.6	0.27
	AD 4.5	0.178	0.158	0.198	5.2	15.3	1690	163	3.7	0.8	14.4	0.36
BF3	16	0.539	0.567	0.685	5.9	51.9	6070	555	12.5	8.5	92.1	0.29
	30	0.946	1.031	1.263	6.1	91.6	11040	981	22.1	28.8	194	0.23

Table 3. PIV ensemble size (number of image pairs)

Pump frequency, $f$ [Hz]	Ensemble size	Number of flow- through times
4.5	750	~650
8	1000	~1500
16	3000	~8670
30	4000	~21780

## 2.5 Flow Characteristics and Variability due to Biofilm Presence

Despite maintaining very similar experimental conditions in the three flow experiments conducted in the presence of biofilm, due to unavoidable differences in biofilm growth, the flow was inherently subject to some degree of variability. Under these conditions, data repeatability was

difficult to achieve. As such, the first step in the present analysis was to statistically characterize the boundary layer by computing the ensemble-averaged profiles and quantifying the variability between the three different sets of experiments. The results presented from biofilm experiments, unless noted otherwise, are the average of the three separate experimental datasets: *BF1*, *BF2* and *BF3* in Table 2, and the error bars for flow over the biofilm beds represent the range of measurements. Individual results are provided as Supporting Information for completeness.

### 3 Results

The results and analysis presented in the following sections are focused on  $f = 4.5$  Hz ( $Re = 1700 \pm 100$ ) and  $f = 30$  Hz ( $Re = 11150 \pm 700$ ), selected to illustrate the main trends observed in the data. Similar behavior was observed for the two intermediate flow rates, whose results are presented as Supplementary Information. In order to facilitate comparison, flow and turbulence variables are presented in dimensionless form; streamwise and wall-normal velocity components are normalized with bulk velocity,  $U_b$ , and Reynolds and form-induced stresses are normalized with  $(u_t^p)^2$ .

#### 3.1 Biofilm Detachment

##### 3.1.1 Imaging Analysis

The flow experiments in the water channel were carried out at different flow rates where the biofilm was subjected to increased shear stress in several incremental stages (Figure 5). This led to progressive detachment of the biofilm from the solid surfaces. For each flow rate, the extent of biofilm that remained attached to the cylinders was measured using a semi-quantitative image processing method using the raw PIV images. At each image pixel, the maximum and minimum pixel intensity within each time series was identified. Next, a map of the difference, or range, between these two values at each pixel (range = max – min) was generated. The low values in this map correspond to portions of the image where particles cannot be present; i.e. the solid cylinder and biofilm, whereas the high values correspond to regions of the image where tracer particles were present intermittently. The range image for the highest pump frequency,  $f = 30$  Hz ( $Re = 11150 \pm 700$ ), in each dataset was taken as the reference. This was done because after this flow stage nearly all biofilm on the top row of cylinders was detached and its visible biofilm coverage in the top layer was nearly non-existent. The

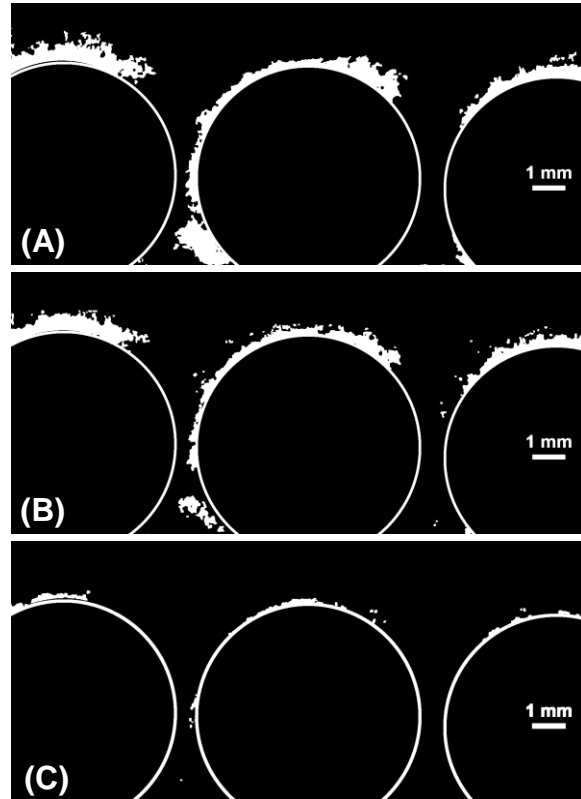


Figure 6. Biofilm coverage at different  $Re$  during the ramp-up stage (A)  $f = 4.5$  Hz ( $Re = 1700 \pm 100$ ), (B)  $f = 8$  Hz ( $Re = 3000 \pm 200$ ), (C)  $f = 16$  Hz ( $Re = 5800 \pm 400$ ). The cylinders are outlined in white and a 1-mm scale bar is shown for reference.

difference calculated with respect to this reference image, and binarized subsequently, depicts the biofilm coverage on the cylinders.

Figure 6 shows the biofilm obtained using this method for a representative dataset. At the beginning of the experiment with the lowest flow rate,  $f = 4.5$  Hz ( $Re = 1700 \pm 100$ ), the biofilm was in a nearly-pristine condition (Figure 6A) as wall shear stress was low and hence detachment was insignificant. As the flow rate was increased, at  $f = 8$  Hz ( $Re = 3000 \pm 200$ ), a modest amount of biofilm detachment was observed (Figure 6B). Finally, at the 2<sup>nd</sup> highest pump frequency of  $f = 16$  Hz ( $Re = 5800 \pm 400$ ), the biofilm coverage was dramatically reduced (Figure 6C). It should be noted that in this way, the biofilm was visualized *indirectly* using the fluorescent particles in raw PIV images. Nevertheless, this method does yield a qualitative picture of the biofilm coverage, since at the end of the experiment biofilm coverage on the top of the cylinders appeared minimal and barely visible to the naked eye. Based on the images, the biofilm thickness on the cylinder crests can be estimated roughly as 0.5–1 mm, 0.25–0.75 mm, and 0.1–0.25 mm at 4.5 Hz, 8 Hz, and 16 Hz, respectively.

### 3.1.2 Effect of Biofilm Detachment on Flow Statistics

Results for flow over beds with different biofilm conditions were compared to quantify the effect of presence of biofilm and biofilm detachment. Comparisons were made at the pump frequency of  $f = 4.5$  ( $Re = 1700 \pm 100$ ) at the beginning and end of each run, corresponding to ramp-up and ramp-down stages, respectively (c.f. Figure 5). The lowest pump frequency was selected for this purpose because of the near-pristine condition of the biofilm at the beginning of the experiment; hence, the biggest difference in biofilm coverage between before and after detachment cases. Figures 7 and 8 compare double-averaged flow statistics for three cases: no biofilm (nBF-45%), biofilm before detachment (BF-BD), and biofilm after detachment (BF-AD). The biofilm data is the average of two independent runs (BF1 and BF2), and the error bars indicate the data range.

Double averaged streamwise and wall-normal velocity profiles, normalized with bulk velocity,  $U_b$  are presented (Figure 7). The streamwise velocity profile for flow over the beds with and without biofilm are highly similar. One difference though is the slight increase in the maximum streamwise velocity ( $U_{max}/U_b$ ) in the presence of biofilm of the free flow at constant flow rate (Figure 7A). The wall normal velocity (Figure 7B), showed an upward motion below the cylinder crests for both BD and AD which was not observed for nBF.

The dimensionless streamwise Reynolds normal stress,  $\langle \overline{u'u'} \rangle / (u_\tau^p)^2$ , at constant pump frequency (Figure 8A) collapsed for  $0.5 \lesssim y/d \lesssim 1$ . Closer to the bed interface, for  $0 \lesssim y/d \lesssim 0.5$ , the stress was highest for the bed without biofilm (nBF) and lowest for biofilm before detachment (BF-BD). The maximum stress occurred at  $y/d \approx 0$  for all configurations.

The dimensionless wall-normal Reynolds normal stress,  $\langle \overline{v'v'} \rangle / (u_\tau^p)^2$ , at constant pump frequency (Figure 8B) collapsed for  $0.4 \lesssim y/d \lesssim 1$ . Close to the bed, for  $0 \lesssim y/d \lesssim 0.4$ , similar to the streamwise Reynolds normal stress, the non-biofilm bed had the highest stress, however, there was very minor difference between the before-detachment (BF-BD) and after-detachment configurations (BF-AD). For nearly all vertical positions, the before and after-detachment configurations (BF-BD and BF-AD) had nearly identical profiles. The peak stress for nBF and

BF-AD occurred at  $y/d \approx 0.25$ , while the peak for BF-BD occurred at a slightly higher coordinate at  $y/d \approx 0.3$ .

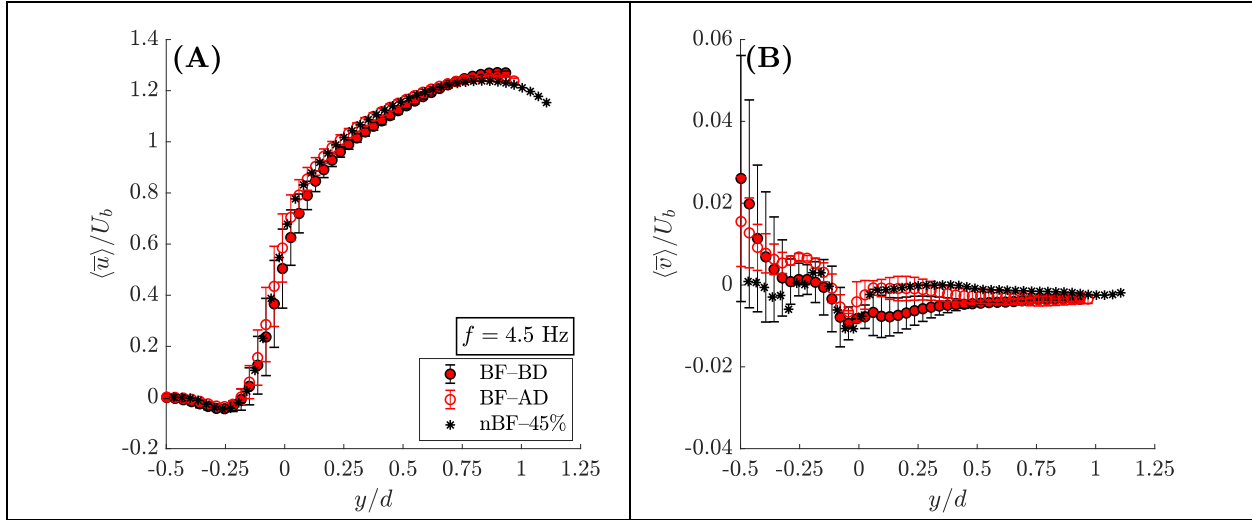


Figure 7. Effect of biofilm detachment on (A) streamwise, and (B) wall-normal velocity. Biofilm before detachment (BF-BD, filled red circle), and after detachment (BF-AD, open red circle), no biofilm (black asterisk). The error bars indicate the range of data for biofilm datasets. The biofilm data (“BF-BD” and “BF-AD”) are from *BF1* and *BF2* datasets. Values of  $U_{max}$  for the presented data are, nBF-45: 0.19 m/s; BF-BD: 0.21 m/s and 0.21 m/s; BF-AD: 0.20 m/s and 0.21 m/s.

Similar to the other components of Reynolds stress presented herein, the dimensionless Reynolds shear stress,  $-\langle \bar{u}'\bar{v}' \rangle / (u_t^p)^2$ , was highest for the bed without biofilm in the range  $0 \lesssim y/d \lesssim 0.5$  (Figure 8C). The profiles collapsed for  $0.5 \lesssim y/d \lesssim 1$ , although within this range, the BF-BD had slightly higher stress values. The biofilm before and after detachment had highly similar profiles, except in the  $-0.1 \lesssim y/d \lesssim 0.3$  range where the normalized RSS after detachment (AD) was higher by approximately 10%. The peak for nBF-45% was at  $y/d \approx 0$ , whereas the peak for both BF-BD and BF-AD occurred at  $y/d \approx 0.18$ .

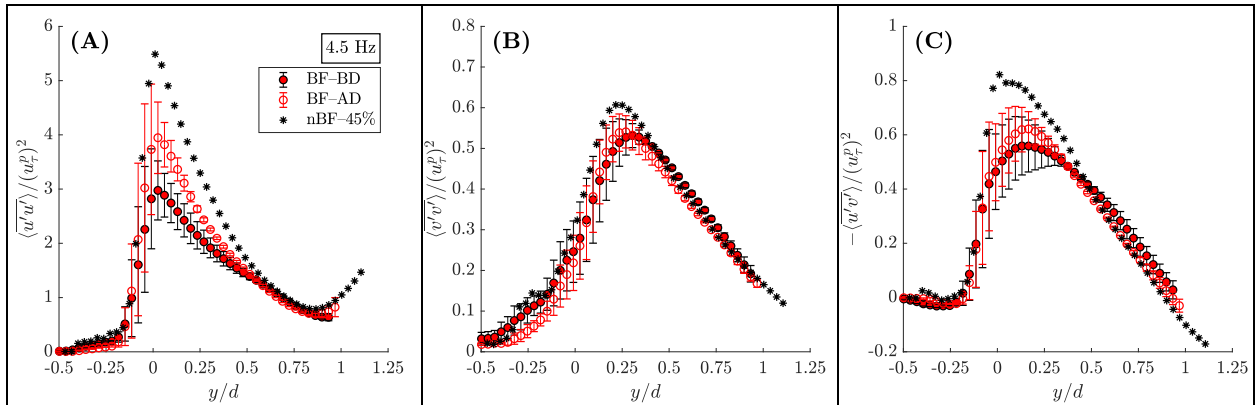


Figure 8. Effect of biofilm presence and subsequent detachment on dimensionless Reynolds stresses. (A) streamwise Reynolds normal stress, (B) wall-normal Reynolds normal stress, and (C) Reynolds shear stress. Biofilm before detachment (BF-BD, filled red circle), biofilm after detachment (BF-AD, open red circle), no biofilm (nBF, black asterisk). The error bars indicate the range of data for biofilm datasets.

### 3.2 Biofilm and Reduced Bed Porosity

One of the potential effects of biofilm growth in a porous bed is a reduction of porosity likely concomitant with reduction in permeability due to blocking of the pores. As described in the previous section, biofilm detachment occurred due to flow shear during experiments. Since shear stress above the bed is larger than stress within the bed, detachment is expected to occur mostly in the top layers of the bed while biomass in the bottom layers of the bed is less affected. It is reasonable to conjecture that the effects described in §3.1.2 were, at least in part, induced by this reduction in pore space size that was maintained even after the ramp-up phase of the experiment, as qualitatively observed in §3.1.1. In an attempt to replicate the effect of reduced bed porosity associated with biofilm presence, and thus test this hypothesis, flow measurements were performed using a permeable bed section with no biofilm but with a lower porosity. In this manner, the experiments aimed to decouple any changing bed porosity from other effects arising from the presence of biofilms, such as roughness and dynamic geometry. Given that the porosity of the bed with biofilm was not quantified, only *partial* decoupling was possible. It should be noted that, in order to maintain the incoming flow configuration as close to the case of flow with biofilm as possible, the porosity of boundary layer development section of the bed was kept at 45%, and only in the test section was porosity reduced to 35%. This created a transition at the beginning of the test section resulting in developing flow.

The double-averaged profiles of streamwise and wall-normal velocity for the two non-biofilm datasets (nBF-45% and nBF-45-35%), and the biofilm averaged data are presented (Figure 9). The streamwise velocity profiles are highly similar and collapse in the outer layer ( $0.5 \lesssim y/d \lesssim 1$ ) for both biofilm and non-biofilm beds. Variations are evident among the biofilm datasets in the inner layer and slightly below the cylinder crest for  $-0.2 \lesssim y/d \lesssim 0.5$ . One notable feature as was observed in the before and after detachment cases (Figure 7A) was the slight increase in the  $U_{max}/U_b$  ratio for the biofilm datasets. A similar, albeit smaller increase is also observed for the non-biofilm reduced porosity bed.

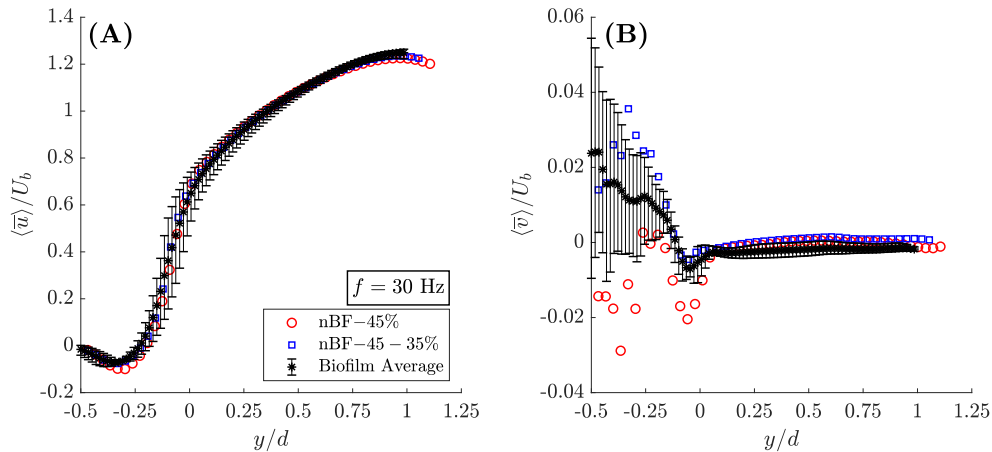


Figure 9. Biofilm effect comparison with reduced bed porosity on streamwise velocity (A, B), and wall-normal velocity (C, D). No biofilm with 45% bed porosity (red circle), no biofilm with 45% porosity in the flow developing section and 35% in the test section (blue square), biofilm (black asterisk). The error bars indicate the range of data for biofilm datasets. Values of  $U_{max}$  for the presented data are, nBF-45%: 1.20 m/s; nBF-45-35%: 1.22 m/s; BF: 1.40 m/s, 1.30 m/s, and 1.26 m/s. ( $Re = 11150 \pm 700$ ),

The wall-normal velocity above the cylinder crest ( $y/d > 0$ ) for all datasets show a near zero velocity, indicating purely horizontal flow. However, there was an upward velocity below the cylinder-tops ( $y/d < 0$ ) for both the reduced porosity bed (nBF-45-35%) and the biofilm bed. This behavior was also observed comparing before and after-detachment at  $f = 4.5$  Hz (Figure 7B).

The log law (Eq. (8)) was fitted to the double-averaged streamwise velocity profile following the method by Fang et al. (2018) (Figure 10). The fitting parameters for all datasets are provided in Table 2. The results show increased equivalent wall roughness height  $k_s^+$  and  $y_0^+$  for the biofilm bed compared to the two no biofilm cases.

Figure 11 presents the double-averaged dimensionless Reynolds stresses for the two datasets without biofilm (nBF-45% and nBF-45-35%), along with the biofilm average. A common feature of the profiles presented herein is that at fixed pump frequency, individual Reynolds stress components (streamwise, wall-normal, and shear) normalized with  $(u_\tau^p)^2$  collapse for all bed configurations in the outer layer  $0.25 \leq y/d \leq 1$ . Near the permeable bed ( $0 \leq y/d \leq 0.25$ ) the reference non-biofilm bed (nBF-45%) has the highest stress. Moreover, the non-biofilm reduced porosity bed (nBF-45-35%) and the biofilm average had highly similar profiles at nearly all  $y$  positions.

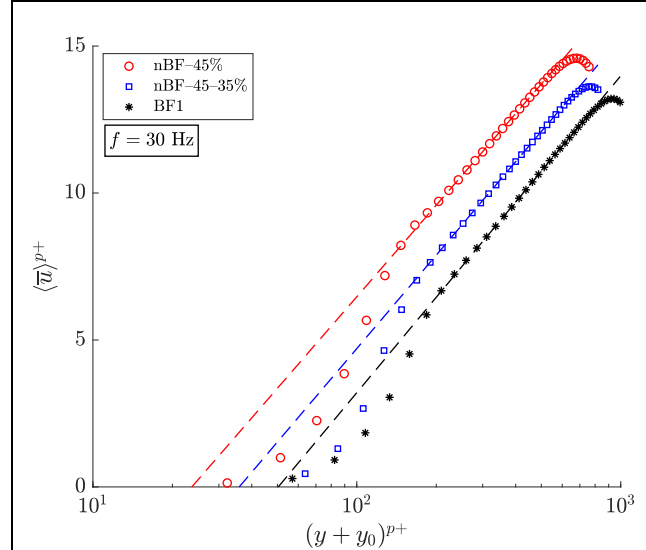


Figure 10. Logarithmic fit to the double-averaged streamwise velocity profiles for 30 Hz pump frequency ( $Re = 11150 \pm 700$ ). Red:  $k_s^+ = 23.7$  for  $y^+ \in [83 \ 350]$ , Blue:  $k_s^+ = 35.9$  for  $y^+ \in [52 \ 388]$ , Black:  $k_s^+ = 50.4$  for  $y^+ \in [112 \ 492]$ . Refer to Table 1 for detailed dataset information.

The dimensionless streamwise Reynolds normal stress,  $\langle u'u' \rangle / (u_\tau^p)^2$ , collapsed for  $0.25 \leq y/d \leq 1$  for the three bed configurations (Figure 11A). Also, the maximum streamwise Reynolds normal stress occurred slightly below the crest at  $y/d \approx -0.1$  for all flow configurations. However, while the reference non-biofilm bed (nBF-45%) had a prominent peak, the reduced porosity non-biofilm bed (nBF-45-35%) and the biofilm bed (BF) had nearly flat and highly similar profiles within the  $-0.1 \leq y/d \leq 0.25$  range. Within this range, the nBF-45% bed had the highest value of  $\langle u'u' \rangle / (u_\tau^p)^2$ .

The dimensionless wall-normal Reynolds normal stress,  $\langle v'v' \rangle / (u_\tau^p)^2$ , for the three bed configurations collapsed for  $y/d \geq 0.4$  (Figure 11B). For  $-0.5 \leq y/d \leq 0.3$ , the reference non-biofilm bed (nBF-45%) had the highest stress values. Also, nBF-45% had a maximum below the cylinder crests at  $y/d \approx -0.1$ , while BF and nBF-45-35% attained their maximum above the bed at  $y/d \approx 0.2$ . The non-biofilm reduced porosity bed (nBF-45-35%) and the biofilm average had nearly identical profiles for all  $y$  positions.

The dimensionless Reynolds shear stress profiles,  $-\langle u'v' \rangle / (u_\tau^p)^2$ , demonstrate a trend similar to the other Reynolds stress components, where the profiles collapsed for  $y/d \geq 0.4$  (Figure 11C). For  $-0.2 \leq y/d \leq 0.4$ , nBF-45% had the highest stress compared to the two other datasets. Moreover,



while the reduced porosity non-biofilm bed (nBF-45-35%) and the biofilm bed had relatively flat profiles for  $-0.1 \lesssim y/d \lesssim 0.25$  and a maximum near  $y/d \approx 0.2$ , the reference non-biofilm bed (nBF-45%) had a prominent peak at  $y/d \approx -0.1$ .

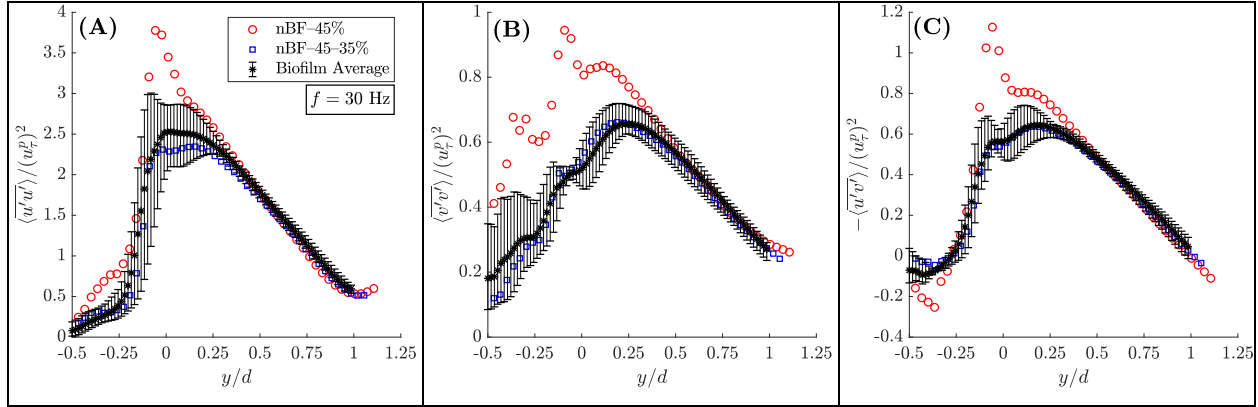


Figure 11. Biofilm effect comparison with reduced bed porosity for  $f = 30$  Hz ( $Re = 11150 \pm 700$ ). (A) streamwise Reynolds normal stress, (B) wall-normal Reynolds normal stress, and (C) Reynolds shear stress. No biofilm with 45% bed porosity (red circle), no biofilm with 45% porosity in the flow developing section and 35% in the test section (blue square), biofilm (black asterisk). The error bars indicate the range of data for biofilm datasets.

The form-induced (dispersive) stresses are presented in Figure 12. In all cases, the form-induced stresses are very small right above the cylinder crests ( $0 \lesssim y/d \lesssim 0.25$ ) and practically zero for  $y/d \gtrsim 0.25$ . Comparing Figures 11 and 12 shows that above the cylinder crests, the form-induced stresses are negligible compared to Reynolds stresses. However, below the crests ( $-0.5 \lesssim y/d \lesssim 0$ ) the form-induced stresses are comparable to Reynolds stresses in magnitudes and cannot be neglected.

The streamwise form-induced normal stresses attain their peak at  $y/d \approx -0.12$ , with a magnitude comparable to that of the corresponding local Reynolds stress (Figure 12A). The wall-normal form-induced normal stresses attain their maximum at  $y/d \approx -0.3$ , where the peak value is even greater than the corresponding local Reynolds stress (Figure 12B). Lastly, the form-induced shear stress showed a behavior and range similar to the Reynolds shear stress within the  $-0.5 \lesssim y/d \lesssim 0$

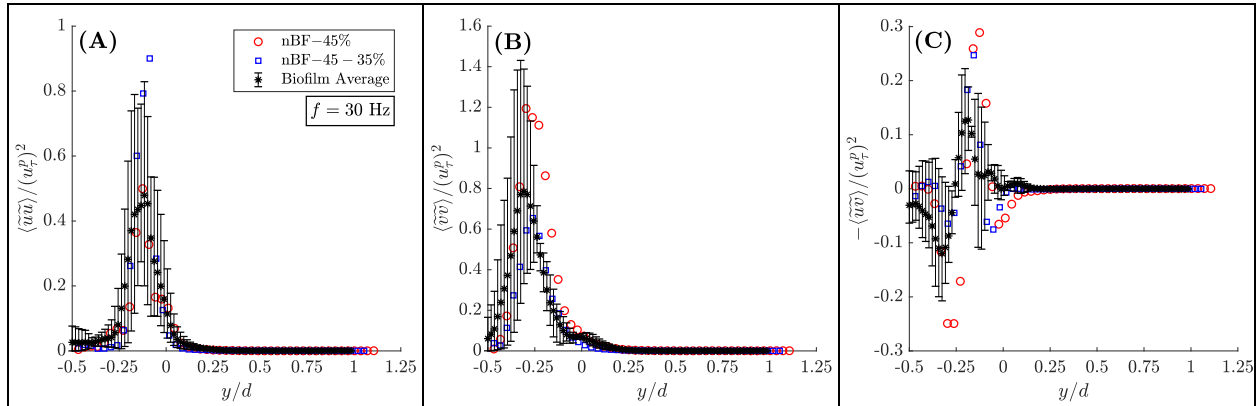


Figure 12. Biofilm effect comparison with reduced bed porosity for  $f = 30$  Hz ( $Re = 11150 \pm 700$ ). (A) streamwise form-induced normal stress, (B) wall-normal form-induced normal stress, and (C) form-induced shear stress. No biofilm with 45% bed porosity (red circle), no biofilm with 45% porosity in the flow developing section and 35% in the test section (blue square), biofilm (black asterisk). The error bars indicate the range of data for biofilm datasets. ( $Re = 11150 \pm 700$ ),

range (Figure 12C). For all components of the form-induced stress, the biofilm datasets demonstrate a broad range of variation that was not observed in Reynolds stresses.

The correlation coefficient ( $-\langle u'v' \rangle / u'_{\text{rms}} v'_{\text{rms}}$ ) of the velocity fluctuations  $u'$  and  $v'$ , is a measure of the efficiency of wall-normal motion in transporting streamwise momentum (Figure 13A). The results indicate that at both  $Re$ , the coefficient has a nearly constant value of  $\sim 0.5$  for  $0 \lesssim y/d \lesssim 0.6$ , and a peak at  $y/d \approx -0.1$ . The value of the peak decreases with porosity and is nearly flat for both the biofilm average and the non-biofilm reduced-porosity bed (nBF-45-35%).

### 3.3 Quadrant Analysis

Quadrant analysis of the instantaneous velocity fields was performed to gain further insight into trends observed in the RSS (Wallace 2016). In this approach,  $u'v'$  is classified into four categories, termed quadrants (Q), based on the sign of  $u'$  and  $v'$ : Q1 ( $u' > 0, v' > 0$ ), Q2 ( $u' < 0, v' > 0$ ), Q3 ( $u' < 0, v' < 0$ ), and Q4 ( $u' > 0, v' < 0$ ), where Q2 and Q4 events are referred to as ejections and sweeps, respectively, and Q1 and Q3 events are called outward and inward interactions. The hyperbolic hole size method of Lu and Willmarth (1973), with a hole size of  $\eta = 4$  has been applied herein. Thus, the intense Reynolds-stress-producing events above the  $\eta = 4$  threshold have been considered. In this configuration, contributions from Q2 and Q4 were stronger than that of Q1 and Q3 by a factor of  $>10$ , so only data for Q2 and Q4 are considered herein. For the flow with biofilm, only one of the three separate datasets has been considered (BF1).

The contributions from Q2 and Q4 to the Reynolds shear stress, non-dimensionalized with  $(u'_t)^2$  and in absolute units are presented in Figure 14A and B, respectively. For the biofilm bed the Q2 and Q4 contributions shift in +y-direction compared to the non-biofilm datasets. The crossover between Q2 and Q4 contributions for the two non-biofilm beds (nBF-45% and nBF-45-35%) occurred at  $y/d \approx 0$ , while for the biofilm bed (BF1) the crossover occurred at  $y/d \approx 0.2$ . Similarly, while Q4 contributions had a maximum near  $y/d \approx -0.1$  for the non-biofilm beds, the peak for BF1 occurred closer to the cylinder crests at  $y/d \approx -0.05$ . The peak for contributions from Q2 events occurred at  $y/d \approx 0.4$  for the nBF-45% dataset and at  $y/d \approx 0.5$  for nBF-45-35% and BF1 datasets. In absolute units, the Q4 contributions (Figure 14B) for the two non-biofilm beds were in relatively close agreement, while BF1 had a wider and taller peak compared to the two non-biofilm datasets. Also, the Q2 contributions for flow over the biofilm bed were stronger than both non-biofilm beds for  $0.25 \lesssim y/d \lesssim 1$ . Thus, for nearly all vertical positions, the intense Q2 and Q4 Reynolds shear stresses for BF1 were stronger than the two nBF datasets, except for  $0 \lesssim y/d \lesssim 0.2$  where nBF-45% had a higher Q2 Reynolds shear stress contribution.

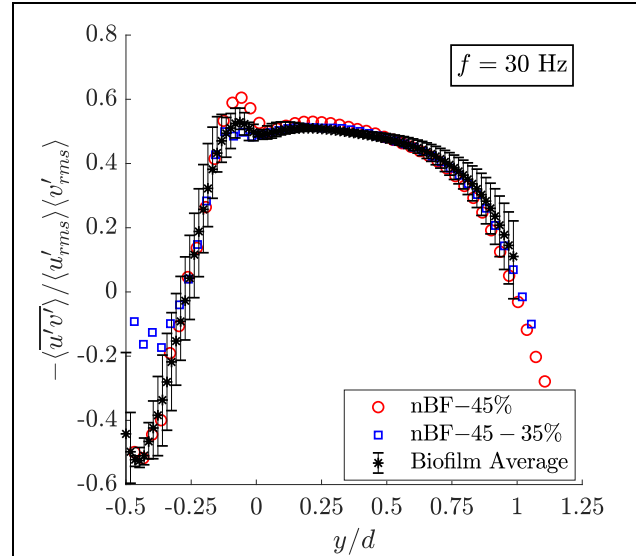


Figure 13. Biofilm effect comparison with reduced bed porosity on correlation coefficient of velocity fluctuations for  $f = 30$  Hz ( $Re = 11150 \pm 700$ ). No biofilm with 45% bed porosity (red circle), no biofilm with 45% porosity in the flow developing section and 35% in the test section (blue square), biofilm (black asterisk).

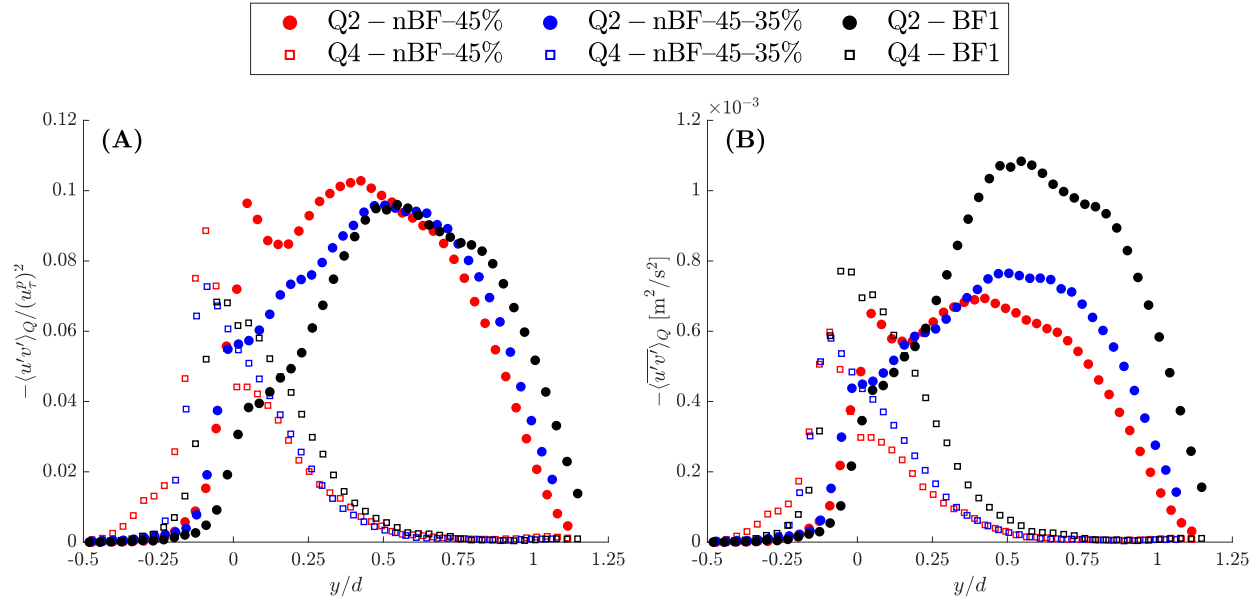


Figure 14. Quadrant analysis showing the distribution of high-intensity Q2 and Q4 (Hole size,  $\eta = 4$ ) for  $f = 30$  Hz ( $Re = 11150 \pm 700$ ). (A) Normalized with  $(u_t^p)^2$ , and (B) in absolute units.

#### 4 Discussion

In comparing flow with and without biofilm at constant pump frequency,  $f$ , the present results show that flow over a bed with biofilm had higher maximum double-averaged streamwise velocity ( $U_{max}$ ) above the bed compared to the no biofilm case. This increase in  $U_{max}$  was concomitant with an increase in bulk velocity,  $U_b$ , resulting in highly similar velocity profiles for the biofilm and non-biofilm beds (Figure 7A and Figure 9A). The increase in  $U_b$  in the presence of biofilm is expected based on the reduction in bed porosity while the total volumetric flow rate,  $Q$ , measured by the flow meter, remained nearly constant.

The double-averaged wall-normal velocity,  $\langle \bar{v} \rangle$ , in all cases, was very close to zero, for  $y/d \gtrsim 0.25$ , indicating a purely horizontal flow, as would be expected. Also, the before and after detachment (BF-BD and BF-AD) profiles were qualitatively similar. In all cases of flow over the biofilm bed and the non-biofilm reduced porosity bed (nBF-45-35%), the profile showed a weak upward velocity for  $-0.5 \lesssim y/d \lesssim -0.1$  (Figure 7B and Figure 9B). The occurrence of the upward motion was likely due to the experimental configuration with a transition in bed porosity at the test section, as explained in §2.1. This apparent channeling of flow from the permeable bed to the free flow was observed in all cases except for the nBF-45% case where the entire bed had constant porosity.

The logarithmic fit to the streamwise velocity profile, Eq. (8), yielded dimensionless equivalent roughness height ( $k_s^+$ ) and zero displacement height ( $y_0^+$ ) that are smaller for the biofilm after detachment (BF-AD) compared to the before detachment (BF-BD) case, at constant pump frequency. In a similar manner, comparing flow with and without biofilm (Figure 10), revealed consistent increase in  $k_s^+$  and  $y_0^+$  in the presence of biofilm. Moreover, for all flow conditions  $y_0^+$  increased with  $Re_K$  consistent with previous results by Suga et al. (2010) and Fang et al. (2018).

The von Karman constant for the logarithmic fit,  $\kappa$ , also decreased with increasing  $Re_K$  with and without biofilm, consistent with previous studies (Fang et al. 2018; Nezu 2005; Suga et al. 2010). However, we should point out there are a few exceptions to this trend. Specifically, when comparing the flow without biofilm over the reduced porosity bed (nBF-45-35%) and the reference flow (nBF-45%) at constant pump frequency,  $y_0^+$  and  $k_s^+$  increased and  $\kappa$  decreased with decreasing bed permeability. Although we cannot determine the exact reason for this behavior, we speculate this effect to be due to the developing nature of flow in nBF-45-35%.

The biofilm coverage depicted in Figure 6 shows a gradual decrease in biofilm coverage due to detachment from flow shear. Unlike the velocity profiles that were not affected significantly by biofilm detachment, the Reynolds stresses experienced a more pronounced impact. Taking together the results from flow over the biofilm bed before and after detachment (Figure 8) as well as with and without biofilm (Figure 11), it is observed that at constant pump frequency, the Reynolds stresses, scaled with  $(u_\tau^p)^2$  for  $0.4 \lesssim y/d \gtrsim 1$  (outer layer). Close to the bed surface  $0 \lesssim y/d \lesssim 0.4$  (inner layer) this scaling fell apart, where in all cases, the dimensionless Reynolds stresses, were dampened in the presence of biofilm. Moreover, for flow over the biofilm bed, as well as the reduced porosity bed (nBF-45-35%), the maximum Reynolds shear stress (Figure 8C) occurred higher above the cylinder crest at  $y/d \approx 0.1$ , compared to  $y/d \approx 0$  for the reference non-biofilm bed. This trend was consistent with the effect of decreased bed porosity observed in previous studies (Breugem et al., 2006).

The quadrant analysis of Reynolds shear stress contributions with a hole size of  $\eta = 4$  showed that for all bed configurations, sweep (Q4) events were strongest near the bed, while ejection events (Q2) were dominant away from the bed surface, for all flow configurations (Figure 14). This was expected from previous studies of flow over permeable beds (Suga et al. 2011). The quadrant analysis reveals that the decrease in dimensionless Reynolds shear stress in the inner layer, in the presence of biofilm, stems primarily from a reduction in Q2 contributions for  $0 \lesssim y/d \lesssim 0.5$ , offset by a modest increase in Q4 contributions.

The form-induced stresses were all nearly zero and practically negligible above the cylinder crests for all datasets. This is in contrast to the findings from (Fang et al. 2018; Manes et al. 2009; Pokrajac et al. 2007). This effect is likely due to the shallow submergence ratio of the roughness elements to the flow depth. To facilitate comparison with studies in open channels, the effective flow depth can be taken as  $y_{max}$  (i.e. distance of maximum  $\langle \bar{u} \rangle$  from the cylinder crest). Hence, the  $d/y_{max}$  ratio in the present study is  $\sim 1$ . Whereas the flow depth to roughness height ratio was 3.5 in Fang et al. (2018), 6–15 in Pokrajac et al. (2007) and 1.67–3.5 in Manes et al. (2009). Below the cylinder crests, for  $-0.5 \lesssim y/d \lesssim 0$ , the form-induced stress terms were significant and, in some instances, greater than their Reynolds stress counterparts. The biofilm datasets had a wide range of variation that can translate to increase or decrease in form-induced stresses relative to the non-biofilm beds. This illustrates the fact that, compared to Reynolds stresses, form-induced stresses are more sensitive to inter-dataset variations.

The peak value of the correlation coefficient (Figure 13) of  $\sim 0.5$  near the cylinder crest was similar to that of flow observed at the top of a vegetation canopy. Notably, while there is not a universal profile for correlation coefficient for different vegetation canopies, the value at the canopy top from studies in different configuration all fall within the range 0.4–0.5 (Finnigan, 2000).

Moreover, the decreased correlation coefficient for flow over a biofilm bed as compared to case without biofilm was similar to the effect expected with reduced bed porosity (Breugem et al., 2006).

In assessing the impact of biofilm presence on flow over a permeable bed with a given geometry, at least two competing effects may be considered: 1) reduced bed porosity concomitant with a likely reduction in bed permeability, and 2) increased roughness and change in geometry of the top of the cylinders. Reduced bed porosity/permeability has a damping effect on Reynolds stresses (Breugem et al., 2006; Suga et al., 2010) while increased roughness has the opposite effect. Studies on flow over smooth impermeable walls have shown that the equivalent roughness for biofilm is larger than its physical roughness, owing to its motion in the flow (Schultz et al., 2015). To test the impact of reduced bed porosity, but without any roughness effect, we used a permeable test module with reduced porosity (35% instead of 45%) but with the same roughness using the same arrangement of cylinders in the top layer (Figure 1G). Interestingly, at constant pump frequency of  $f = 30$  Hz, the dimensionless Reynolds stress profiles (Figure 11) showed close agreement between the non-biofilm reduced porosity bed (nBF-45-35%) and the biofilm average, whereas this was not the case at lower frequencies. This is in part due to the fact that at the highest tested flow rate the biofilm coverage on cylinder crests was mostly detached, while some biofilm remain attached at lower pumping frequencies (c.f. Figure 6). Unlike the Reynolds stresses, the form-induced stresses (Figure 12), which are dominant below the cylinder crests, showed significant difference between the non-biofilm reduced porosity bed (nBF-45-35%) and the biofilm beds.

An important point to note here is that comparison of different studies is not a straightforward task, primarily due to the unique nature of different experimental configurations in terms of bed configuration (porosity, grain size) as well as biofilm coverage and growth method. In particular, there are very few studies with velocity measurements over *permeable* beds *with* biofilm. Our results indicate higher wall shear stress as a result of presence of biofilm in flow over a permeable bed (Table 2). However, in open channel flow over rough *impermeable* beds with 20-mm tall hemispheres, Graba et al. (2010) showed that biofilm growth results in slightly lower wall shear stress. Nikora et al. (2002) used a nearly identical rough impermeable geometry as that used by Graba et al. (2010) and reported no change in wall shear stress. One major difference between the present study and both Graba et al. (2010) and Nikora et al. (2002) is that the rough wall was impermeable in these previous studies, which is not representative of natural gravel-bed rivers. Another factor worthy of note is the extent of biofilm growth and coverage. In the study of Graba et al. (2010), the biofilm occupied the space between the hemispherical roughness elements (pebbles), whilst in Nikora et al. (2002) biofilm covered the entire bed as a thick mat, thus completely changing the nature of the roughness and the bed. However, in the current study the biofilm remained as a heterogenous film covering the cylinders but without connecting the adjacent cylinders (at least in the top row which was easily visible). Moreover, the increased wall-normal Reynolds normal stress in absolute units in the presence of biofilm reported herein are in contrast to results from Vignaga et al. (2013). This discrepancy can be attributed to the experimental configuration, as Vignaga et al. (2013) conducted their experiments with 20-mm-deep beds consisting of beads/grains 1–2.2 mm in diameter, and with a free flow depth of 30–40 mm. Their observed decrease in wall-normal velocity fluctuations (no results on streamwise fluctuations or RSS were reported) can be in part attributed to the shallow depth of the bed relative to free flow, as suggested by results of Kim et al. (2018). Moreover, the reduced velocity

fluctuations reported by Vignaga et al. (2013), may be a result of biofilm smoothing the surface, similar to that observed by Graba et al. (2010) and Nikora et al. (2002) as the biofilm growth resulted in a sediment-biofilm composite material.

Figure 15 depicts the key processes involved in flow over a permeable bed with biofilm as studied herein. The main question which we attempted to answer was how the reduced bed porosity and change in roughness combine to modify flow the bed.

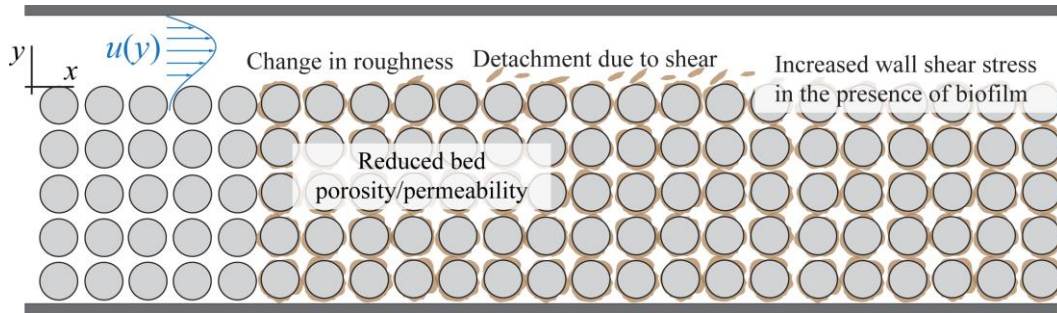


Figure 15. Processes involved in flow over a permeable bed with biofilm as investigated in the present work.

## 5 Limitations and Implications of the Flow Apparatus

The results of this study are inevitably impacted by the choices in the design of the experimental apparatus and protocol. There were potentially important parameters whose impact has not been studied herein. One such effect is the spanwise variations for the BF datasets. While the incoming flow conditions during biofilm development were maintained as uniform as possible in the spanwise direction, there could have been some non-uniformity in biofilm growth and biomass accumulation in the spanwise direction. Specifically, near the side walls the distribution of biomass could be different from the mid-plane.

Another point to mention is that biofilm coverage in the flow channel was limited to a 0.30-m long portion in the test section as biofilm was developed in a standalone recirculating reactor (c.f. §2.2). This was done to avoid undesired biofilm growth in portions of the water channel with limited access for cleaning. Thus, there was a transition in bed geometry at the beginning of the test section. As a result, in the cases of flow with biofilm (BF datasets) and reduced-porosity-bed (nBF-45-35%) the flow was likely not fully developed.

It is also worthy of consideration whether the method of biofilm development (i.e. in a separate reactor at low  $Re$  and shear) had an impact on the results. Due to this approach, the shear stress experienced by the biofilm was significantly higher during the flow experiments than during the growth stage. Vignaga et al. (2013) used a similar approach for part of their experiments to test biofilm at different stages of development. In other studies, however, the biofilm development and growth were carried out under same flow conditions (i.e.  $Re$  and shear) as the flow experiments. The significance of this difference is increased attachment and cohesive strength of biofilms developed under high shear (Stoodley et al., 2002), resulting in a denser biofilm compared to the present study. As a result, in the present study, progressive biofilm detachment occurred as the flow rate was increased. This particular scenario may be similar to that during flood events in



natural channels, where biofilm experience abrupt increases and decreases in flow-induced shear during unsteady flow conditions.

Finally, the flow facility used in the present study consisted of a closed channel, whereas in past studies, (e.g. Graba et al. 2010; Nikora et al. 2002; Vignaga et al. 2013) an open channel was employed. We adopted use of a closed channel with a smooth impermeable top wall herein for the purpose of optical access and better control over boundary conditions. Although the top smooth impermeable wall can dampen pressure fluctuations compared to the case of an open channel flow, turbulence effects are still dominated by the rough permeable bottom wall. Thus, our results can provide insight into the effect of biofilm on flow over a permeable bed. In this regard, we expect the trends observed in Reynolds stresses in the presence of biofilm, as well as before and after biofilm detachment to be applicable (at least qualitatively) to open channel flow with similar  $Re_K$  and  $Re_\tau^p$ .

## 6 Summary and Conclusions

The effect of biofilms on flow structure over a permeable bed was quantified using PIV measurements in a closed-top recirculating channel flow. In order to account for the variability in biofilm growth, three separate biofilm batches were developed and tested. One of the ways that biofilm presence can affect flow over a permeable bed is through a reduction in bed porosity by biomass occupying the pore spaces. This effect was investigated by testing flow over a reduced-porosity bed without biofilm. The results showed that while certain aspects of the effect of biofilm presence on flow can be replicated with reduced bed porosity without biofilm, the effect of biofilm is highly complicated and full understanding of the two-way interaction between flow and biofilms requires further investigations. The following main conclusions can be drawn from the present study:

1. The wall shear stress and friction velocity obtained from the total shear stress increased in the presence of biofilm, and decreased as a result of biofilm detachment, when compared at constant pump frequency.
2. At constant pump frequency, the equivalent roughness height,  $k_s^+$ , and zero displacement height,  $y_0^+$ , were lower for biofilm after detachment (BF-AD) compared to before detachment (BF-BD). Also,  $k_s^+$  and  $y_0^+$  were higher in the presence of biofilm compared to the no biofilm datasets.
3. In all flow configuration studied herein (with and without biofilm) at constant pump frequency, the individual components of Reynolds stresses scaled with  $(u_\tau^p)^2$  for  $\sim 0.4 < y/d < 1$  (outer layer), while the dimensionless Reynolds stresses decreased in the presence of biofilm for  $0 \lesssim y/d \lesssim 0.25$  (inner layer).
4. The quadrant analysis (hole size,  $\eta = 4$ ) suggests that the reduction in dimensionless Reynolds shear stresses in the inner layer in the presence of biofilm is primarily due to a reduction in strong Q2 contributions.

Turbulence plays a major role in mass and momentum exchange across the bed interface between the free and subsurface flow in a wide range of geophysical flows. Our results suggest that models for flow and transport over such permeable media in aquatic environments cannot neglect the role of biofilms in modifying turbulence. In light of observations reported herein, the following are important areas that were not considered in the present study, but we believe must be considered in future investigations:

1. In-situ imaging and quantification of biofilm morphology can help elucidate the two-way coupling between turbulence and biofilm growth/detachment. Distribution of biomass in the span-wise and depth directions of the bed may create non-negligible three-dimensional effects in flow.
2. The interaction between free and subsurface flow in the presence of biofilm is worthy of further investigation. However, non-intrusive measurement and optical access are expected to be major obstacles to investigating flow inside the bed.

## Acknowledgment

We thank the UK Natural Environment Research Council for funding this work (NE/K012819/1), and Monica Ochoa for her help in running and maintaining the biofilm reactor. We are also thankful to the anonymous reviewers whose comments helped improve the paper. All experiments were undertaken in the Department of Aerospace and Mechanical Engineering at the University of Notre Dame. We note that data used in the manuscript is available for download at <https://doi.org/10.3886/E118207V1>.

## References

- Aubeneau, A. F., Brittany Hanrahan, Diogo Bolster, and Jennifer Tank. 2016. "Biofilm Growth in Gravel Bed Streams Controls Solute Residence Time Distributions." *Journal of Geophysical Research: Biogeosciences* 121(7):1840–50.
- Battin, Tom J., Louis A. Kaplan, J. Denis Newbold, and Claude M. E. Hansen. 2003. "Contributions of Microbial Biofilms to Ecosystem Processes in Stream Mesocosms." *Nature* 426(6965):439–42.
- Battin, Tom J., William T. Sloan, Staffan Kjelleberg, Holger Daims, Ian M. Head, Tom P. Curtis, and Leo Eberl. 2007. "Microbial Landscapes: New Paths to Biofilm Research." *Nature Reviews. Microbiology* 5(1):76–81.
- Blois, G., G. H. Sambrook Smith, J. L. Best, R. J. Hardy, and J. R. Lead. 2011. "Quantifying the Dynamics of Flow within a Permeable Bed Using Time-Resolved Endoscopic Particle Imaging Velocimetry (EPIV)." *Experiments in Fluids* 53(1):51–76.
- Blois, G., G. H. Sambrook Smith, J. L. Best, R. J. Hardy, and J. R. Lead. 2012. "Quantifying the Dynamics of Flow within a Permeable Bed Using Time-Resolved Endoscopic Particle Imaging Velocimetry (EPIV)." *Experiments in Fluids* 53(1):51–76.
- Blois, Gianluca, James L. Best, Gregory H. Sambrook Smith, and Richard J. Hardy. 2014. "Effect of Bed Permeability and Hyporheic Flow on Turbulent Flow over Bed Forms." *Geophysical Research Letters* 41(18):6435–42.
- Boano, F., J. W. Harvey, a. Marion, a. I. Packman, R. Revelli, L. Ridolfi, and a. Wörman. 2014. "Hyporheic Flow and Transport Processes: Mechanisms, Models, and Biogeochemical Implications." *Reviews of Geophysics* 1–77.
- Breugem, W. P. and B. J. Boersma. 2005. "Direct Numerical Simulations of Turbulent Flow over



- 748 a Permeable Wall Using a Direct and a Continuum Approach.” *Physics of Fluids*  
749 17(2):025103.
- 750 Breugem, Wim-Paul, B. J. Boersma, and R. E. Uittenbogaard. 2006. “The Influence of Wall  
751 Permeability on Turbulent Channel Flow.” *Journal of Fluid Mechanics* 562:35.
- 752 Cardenas, M. Bayani. 2015. “Hyporheic Zone Hydrologic Science: A Historical Account of Its  
753 Emergence and a Prospectus.” *Water Resources Research* n/a-n/a.
- 754 Carrel, M., V. L. Morales, M. Dentz, N. Derlon, E. Morgenroth, and M. Holzner. 2018. “Pore-  
755 Scale Hydrodynamics in a Progressively Bioclogged Three-Dimensional Porous Medium: 3-  
756 D Particle Tracking Experiments and Stochastic Transport Modeling.” *Water Resources*  
757 *Research* 1–16.
- 758 Dzubakova, Katharine, Hannes Peter, Enrico Bertuzzo, Carmelo Juez, Mário J. Franca, Andrea  
759 Rinaldo, and Tom J. Battin. 2018. “Environmental Heterogeneity Promotes Spatial Resilience  
760 of Phototrophic Biofilms in Streambeds.” *Biology Letters* 14(10):0–3.
- 761 Fang, Hongwei, Xu Han, Guojian He, and Subhasish Dey. 2018. “Influence of Permeable Beds on  
762 Hydraulically Macro-Rough Flow.” *Journal of Fluid Mechanics* 847:552–90.
- 763 Finnigan, John. 2000. “Turbulence in Plant Canopies.” *Annual Review of Fluid Mechanics*  
764 32(1):519–71.
- 765 Graba, Myriam, Frédéric Y. Moulin, Stéphanie Boulêtreau, Frédéric Garabétian, Ahmed Kettab,  
766 Olivier Eiff, José Miguel Sánchez-Pérez, and Sabine Sauvage. 2010. “Effect of Near-Bed  
767 Turbulence on Chronic Detachment of Epilithic Biofilm: Experimental and Modeling  
768 Approaches.” *Water Resources Research* 46(11):n/a-n/a.
- 769 Graba, Myriam, Sabine Sauvage, Frédéric Y. Moulin, Gemma Urrea, Sergi Sabater, and José  
770 Miguel Sanchez-Pérez. 2013. “Interaction between Local Hydrodynamics and Algal  
771 Community in Epilithic Biofilm.” *Water Research* 47(7):2153–63.
- 772 Grant, Stanley B., Jesus D. Gomez-Velez, and Marco Ghisalberti. 2018. “Modeling the Effects of  
773 Turbulence on Hyporheic Exchange and Local-to-Global Nutrient Processing in Streams.”  
774 *Water Resources Research* (1):5883–89.
- 775 Kim, Taehoon, Gianluca Blois, James L. Best, and Kenneth T. Christensen. 2018. “Experimental  
776 Study of Turbulent Flow over and within Cubically Packed Walls of Spheres: Effects of  
777 Topography, Permeability and Wall Thickness.” *International Journal of Heat and Fluid*  
778 *Flow* 73(May):16–29.
- 779 Kim, Taehoon, Gianluca Blois, James L. Best, and Kenneth T. Christensen. 2019. “PIV  
780 Measurements of Turbulent Flow Overlying Large, Cubic- and Hexagonally-Packed  
781 Hemisphere Arrays.” *Journal of Hydraulic Research* 1686.
- 782 Kim, Taehoon, Gianluca Blois, James L. Best, and Kenneth T. Christensen. 2020. “Experimental  
783 Evidence of Amplitude Modulation in Permeable-Wall Turbulence.” *Journal of Fluid*

784 *Mechanics.*

- 785 Labiod, C., R. Godillot, and B. Caussade. 2007. "The Relationship between Stream Periphyton  
786 Dynamics and Near-Bed Turbulence in Rough Open-Channel Flow." *Ecological Modelling*  
787 209(2–4):78–96.
- 788 Lichtman, Ian D., Jaco H. Baas, Laurent O. Amoudry, Peter D. Thorne, Jonathan Malarkey, Julie  
789 A. Hope, Jeffrey Peakall, David M. Paterson, Sarah J. Bass, Richard D. Cooke, Andrew J.  
790 Manning, Alan G. Davies, Daniel R. Parsons, and Leiping Ye. 2018. "Bedform Migration in  
791 a Mixed Sand and Cohesive Clay Intertidal Environment and Implications for Bed Material  
792 Transport Predictions." *Geomorphology* 315:17–32.
- 793 Lu, S. S. and W. W. Willmarth. 1973. "Measurements of the Structure of the Reynolds Stress in a  
794 Turbulent Boundary Layer." *Journal of Fluid Mechanics* 60(03):481.
- 795 Malarkey, Jonathan, Jaco H. Baas, Julie A. Hope, Rebecca J. Aspden, Daniel R. Parsons, Jeff  
796 Peakall, David M. Paterson, Robert J. Schindler, Leiping Ye, Ian D. Lichtman, Sarah J. Bass,  
797 Alan G. Davies, Andrew J. Manning, and Peter D. Thorne. 2015. "The Pervasive Role of  
798 Biological Cohesion in Bedform Development." *Nature Communications* 6:1–6.
- 799 Manes, C., D. Poggi, and L. Ridolfi. 2011. "Turbulent Boundary Layers over Permeable Walls:  
800 Scaling and near-Wall Structure." *Journal of Fluid Mechanics* 687:141–70.
- 801 Manes, C., D. Pokrajac, V. I. Nikora, L. Ridolfi, and D. Poggi. 2011. "Turbulent Friction in Flows  
802 over Permeable Walls." *Geophysical Research Letters* 38(3):n/a–n/a.
- 803 Manes, Costantino, Dubravka Pokrajac, Ian McEwan, and Vladimir Nikora. 2009. "Turbulence  
804 Structure of Open Channel Flows over Permeable and Impermeable Beds: A Comparative  
805 Study." *Physics of Fluids* 21(12):1–12.
- 806 Nakayama, A., F. Kuwahara, and Y. Sano. 2007. "Concept of Equivalent Diameter for Heat and  
807 Fluid Flow in Porous Media." *AIChE Journal* 53(3):732–36.
- 808 Nezu, Iehisa. 2005. "Open-Channel Flow Turbulence and Its Research Prospect in the 21st  
809 Century." *Journal of Hydraulic Engineering* 131(4):229–46.
- 810 Nikora, V. I., D. G. Goring, and B. J. F. Biggs. 2002. "Some Observations of the Effects of Micro-  
811 Organisms Growing on the Bed of an Open Channel on the Turbulence Properties." *Journal*  
812 *of Fluid Mechanics* 450:317–41.
- 813 Nikora, Vladimir, Derek Goring, Ian McEwan, and George Griffiths. 2001. "Spatially Averaged  
814 Open-Channel Flow over Rough Bed." *Journal of Hydraulic Engineering* 127(2):123–33.
- 815 Packman, Aaron I. and K. E. Bencala. 2000. "Modeling Surface-Subsurface Hydrological  
816 Interactions." Pp. 45–80 in *Streams and Ground Waters*.
- 817 Parsons, Daniel R., Robert J. Schindler, Julie A. Hope, Jonathan Malarkey, Jaco H. Baas, Jeffrey  
818 Peakall, Andrew J. Manning, Leiping Ye, Steve Simmons, David M. Paterson, Rebecca J.

- 819 Aspden, Sarah J. Bass, Alan G. Davies, Ian D. Lichtman, and Peter D. Thorne. 2016. “The  
820 Role of Biophysical Cohesion on Subaqueous Bed Form Size.” *Geophysical Research Letters*  
821 43(4):1566–73.
- 822 Pokrajac, Dubravka, Lorna Jane Campbell, Vladimir Nikora, Costantino Manes, and Ian McEwan.  
823 2007. “Quadrant Analysis of Persistent Spatial Velocity Perturbations over Square-Bar  
824 Roughness.” *Experiments in Fluids* 42(3):413–23.
- 825 Pokrajac, Dubravka and Costantino Manes. 2009. “Velocity Measurements of a Free-Surface  
826 Turbulent Flow Penetrating a Porous Medium Composed of Uniform-Size Spheres.”  
827 *Transport in Porous Media* 78(3):367–83.
- 828 Roche, K. R., G. Blois, J. L. Best, K. T. Christensen, A. F. Aubeneau, and A. I. Packman. 2018.  
829 “Turbulence Links Momentum and Solute Exchange in Coarse-Grained Streambeds.” *Water*  
830 *Resources Research* 54(5):3225–42.
- 831 Roche, K. R., J. D. Drummond, F. Boano, A. I. Packman, T. J. Battin, and W. R. Hunter. 2017.  
832 “Benthic Biofilm Controls on Fine Particle Dynamics in Streams.” *Water Resources*  
833 *Research* 53(1):222–36.
- 834 Rosti, Marco E., Luca Cortelezzi, and Maurizio Quadrio. 2015. “Direct Numerical Simulation of  
835 Turbulent Channel Flow over Porous Walls.” *Journal of Fluid Mechanics* 784(2015):396–  
836 442.
- 837 Salant, Nira L. 2011. “‘Sticky Business’: The Influence of Streambed Periphyton on Particle  
838 Deposition and Infiltration.” *Geomorphology* 126(3–4):350–63.
- 839 Schultz, M. P., J. M. Walker, C. N. Steppe, K. A. Flack, J. M. Walker, C. N. Steppe, and K. A.  
840 Flack Impact. 2015. “Impact of Diatomaceous Biofilms on the Frictional Drag of Fouling-  
841 Release Coatings.” *Biofouling* 31(9–10):759–73.
- 842 Sinha, Sumit, Richard J. Hardy, Gianluca Blois, James L. Best, and Gregory H. Sambrook Smith.  
843 2017. “A Numerical Investigation into the Importance of Bed Permeability on Determining  
844 Flow Structures over River Dunes.” *Water Resources Research* 53(4):3067–86.
- 845 Sternecker, Katharina, Romy Wild, and Juergen Geist. 2013. “Effects of Substratum Restoration  
846 on Salmonid Habitat Quality in a Subalpine Stream.” *Environmental Biology of Fishes*  
847 96(12):1341–51.
- 848 Stoesser, Thorsten and Wolfgang Rodi. 2007. “Large Eddy Simulation of Open-Channel Flow  
849 Over Spheres.” Pp. 321–30 in *High Performance Computing in Science and Engineering’06*.  
850 Springer Berlin Heidelberg.
- 851 Stoodley, P., R. Cargo, C. J. Rupp, S. Wilson, and I. Klapper. 2002. “Biofilm Material Properties  
852 as Related to Shear-Induced Deformation and Detachment Phenomena.” *Journal of Industrial*  
853 *Microbiology & Biotechnology* 29(6):361–67.
- 854 Suga, K., Y. Matsumura, Y. Ashitaka, S. Tominaga, and M. Kaneda. 2010. “Effects of Wall

- 855 Permeability on Turbulence.” *International Journal of Heat and Fluid Flow* 31(6):974–84.
- 856 Suga, K., M. Mori, and M. Kaneda. 2011. “Vortex Structure of Turbulence over Permeable Walls.”  
857 *International Journal of Heat and Fluid Flow* 32(3):586–95.
- 858 Suga, Kazuhiko, Yuka Nakagawa, and Masayuki Kaneda. 2017. “Spanwise Turbulence Structure  
859 over Permeable Walls.” *J. Fluid Mech* 822:186–201.
- 860 Vignaga, Elisa, David M. Sloan, Xiaoyu Luo, Heather Haynes, Vernon R. Phoenix, and William  
861 T. Sloan. 2013. “Erosion of Biofilm-Bound Fluvial Sediments.” *Nature Geoscience*  
862 6(9):770–74.
- 863 Walker, J. M., J. E. Sargison, and A. D. Henderson. 2013. “Turbulent Boundary-Layer Structure  
864 of Flows over Freshwater Biofilms.” *Experiments in Fluids* 54(12):1628.
- 865 Wallace, James M. 2016. “Quadrant Analysis in Turbulence Research: History and Evolution.”  
866 *Annual Review of Fluid Mechanics* 48(1):131–58.
- 867